Chapter 11
Planetary Ionospheres and Magnetospheres

11.1 Earth: Ionospheric Layers

Sunlight interacts with planetary atmospheres to produce excited atoms and ions, and the ions interact with each other and with neutral atoms to produce unique, altitude-dependent populations. As with other aspects of the terrestrial planets, we know the ionosphere of the Earth best, so we start with it. Figure 11.1 shows the electron density and ionospheric layers in the Earth's ionosphere. During the daytime, the D layer forms and the F layer separates into two parts, F_1 and F_2; at night the D layer disappears, and the F layers merge into a single layer.

11.1.1 The F Layer

The F layer is created primarily by solar EUV radiation in the wavelength range $10\ \text{nm} < \lambda < 80\ \text{nm}$.

11.1.1.1 Atoms and Ions in the F Layer

The dominant neutral atoms are O and N_2. Atomic oxygen is much more abundant than O_2 in the F region because most of the O_2 has undergone *photodissociation* (or *photolysis*):

$$O_2 + h\nu \rightarrow O + O \quad \text{photodissociation} \tag{11.1}$$

where, as an aid, we list the mechanism after the reaction.

E.F. Milone and W.J.F. Wilson, *Solar System Astrophysics: Planetary Atmospheres and the Outer Solar System*, Astronomy and Astrophysics Library,
DOI 10.1007/978-1-4614-9090-6_2, © Springer Science+Business Media New York 2014

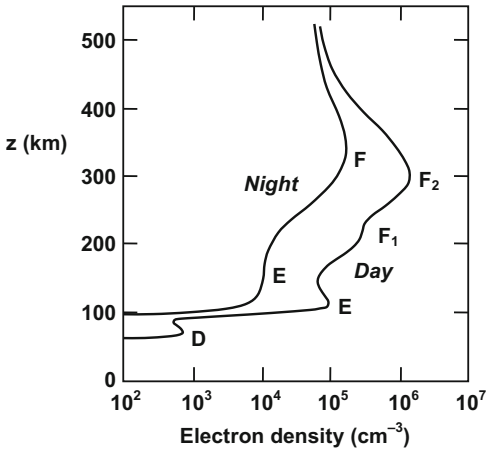

Fig. 11.1 Electron density vs. altitude in the Earth's ionosphere. Typical curves and ionospheric layers are shown for night and day. The curves vary considerably with solar activity, sunspot number, and time of year. From Iribarne and Cho (1980), Fig. I-7, p. 10

11.1.1.2 Production Mechanisms

The dominant ions are primarily O^+ with smaller amounts of O_2^+, NO^+, N^+. The production of the ions is due to several reactions. The dominant (source) reactions are as follows:

A. The primary[1] reactions, the process, and the wavelength range are

$$O + h\nu \rightarrow O^+ + e^- \quad \text{photoionization} \quad \lambda < 91.0 \text{ nm} \tag{11.2a}$$

$$N + h\nu \rightarrow N^+ + e^- \quad \text{photoionization} \quad \lambda < 85.2 \text{ nm} \tag{11.2b}$$

$$N_2 + h\nu \rightarrow N_2^+ + e^- \quad \text{photoionization} \quad \lambda < 79.6 \text{ nm} \tag{11.2c}$$

B. The secondary reactions are

$$N_2^+ + O \rightarrow N_2 + O_2^+ \quad \text{charge transfer} \tag{11.3a}$$

$$N_2^+ + O \rightarrow N + NO^+ \quad \text{ion exchange} \tag{11.3b}$$

Most of the N_2^+ produced in the primary reactions is thus removed by the secondary reactions.

[1] The words "primary" and "secondary" refer to the sequence of events, not to relative importance, i.e., the primary reactions have to occur first, in order for the secondary reactions to occur.

11.1.1.3 Loss Mechanisms

The loss mechanisms (sinks) of the ions are as follows:

A. Molecular ions

The most common process is dissociative recombination, where the electron recombines with a molecule, dissociating it into two neutral atoms in the process:

$$O_2^+ + e^- \rightarrow O + O \quad \text{dissociative recombination} \tag{11.4a}$$

$$NO^+ + e^- \rightarrow N + O \quad \text{dissociative recombination} \tag{11.4b}$$

$$N_2^+ + e^- \rightarrow N + N \quad \text{dissociative recombination} \tag{11.4c}$$

Dissociative recombination is required instead of simple recombination, e.g.,

$$O_2^+ + e^- \rightarrow O_2 \quad \text{recombination} \tag{11.5a}$$

because recombination is an exothermic process: energy is released. $O_2^+ + e^- \rightarrow O_2$ would leave the O_2 with an excess of energy that in fact would dissociate the molecule.

Radiative recombination, e.g.,

$$O_2^+ + e^- \rightarrow O_2 + h\nu \quad \text{radiative recombination} \tag{11.5b}$$

has a low probability and can be ignored compared to dissociative recombination.

B. Atomic ions

Simple recombination of electrons with atomic ions does not occur for the same reason described earlier for molecules: the recombination is an exothermic process, and the excess energy given to the atom by the recombination is sufficient to eject the electron again. The principal loss mechanism for atomic ions is charge transfer to a molecule

$$O^+ + O_2 \rightarrow O + O_2^+ \quad \text{charge transfer} \tag{11.6}$$

followed by molecular dissociative recombination:

$$O_2^+ + e^- \rightarrow O + O \quad \text{dissociative recombination} \tag{11.4a}$$

11.1.1.4 Ion Concentration vs. Altitude

The concentration of a given species of ion at any given altitude in the ionosphere depends on the following:

A. The production rate, which depends on the concentration of the "source" species (there will be, for instance, little O^+ if there is little atomic O to be ionized) and

the amount of ionizing radiation present, which decreases with decreasing altitude because of absorption at higher altitudes.

B. The loss rate, which depends on (among other things) the density of air, because collisions which remove ions through such processes as electron recombination and charge transfer are less frequent at lower densities.

C. The rate of vertical diffusion. Each species of ion tends to redistribute itself according to its own pressure scale height (Sect. 10.5.4.4), resulting in fractionation because lower mass ions have larger scale heights. We can describe two separate regimes, one below and the other above the peak of the F_2 region at 300 km altitude:

   1. $h < 300$ km altitude. Here, the density is "high," so the mean ionic lifetime is "short," and any ions produced are destroyed before they can diffuse to a different altitude. Therefore, below 300 km altitude, the ion concentrations at any given level are controlled primarily by local production and loss. This condition is called *photochemical equilibrium.*
   2. $h > 300$ km altitude. Here, the density is "low," so the mean ionic lifetime is "long," and ions have time to diffuse to different altitudes before they are destroyed. Thus the ion concentrations above 300 km altitude are controlled primarily by *diffusion,* producing an exponential decrease in the number density of each ion with altitude, according to the scale height.

D. Horizontal transport. The Earth's magnetic field, $\vec{B}$, is directed into the ground in the north polar region (e.g., Fig. 11.23), and the magnetospheric processes described in Sect. 11.6.5 create an electric field, $\vec{E}$, from the dawn side of the pole toward the dusk side (see Fig. 11.31). Patches of ionization created in the polar cusp (Fig. 11.23) at F layer altitudes can then undergo $\vec{E} \times \vec{B}$ drift (Sect. 11.5.6) at speeds up to several km/s from there into high latitudes on the nightside. $\vec{E} \times \vec{B}$ drift and related magnetospheric and ionospheric processes are described in detail in Sects. 11.5 and 11.6.

11.1.1.5 Charge Separation

The same processes of diffusion as apply above 300 km altitude and of photochemical equilibrium as apply below 300 km control the concentration of free electrons. Because of their small mass, their scale height is almost infinite compared to the positive ions, and their diffusion produces a vertical charge separation in the ionosphere above 300 km. This *ambipolar diffusion* (diffusion resulting in a charge separation) creates an upward force on the positive ions (especially H^+), lifting them to higher altitudes, so that the scale heights for any ion is about twice the scale height of the equivalent neutral atom.

11.1.2 The E Layer

The E layer is distinct from the F layer by virtue of being created by different wavelengths of solar radiation:

F: primarily 10 nm $< \lambda <$ 80 nm
E: primarily 80 nm $< \lambda <$ 102.6 nm

and is characterized by a different population of neutral atoms and ions.

11.1.2.1 Atoms and Ions in the E Layer

The dominant neutrals are N_2, O_2, and O. Because of UV absorption in the F layer, there is less photodissociation of O_2 in the E layer; so O is less abundant than N_2 and O_2 in all but the highest parts of the E region. The dominant ions are NO^+ and O^+.

11.1.2.2 Production Mechanisms

The production of ions is due to photoionization and other processes: O_2 is more important in the E layer than in the F layer, but otherwise the reactions are similar.

A. The primary reactions (*i.e.,* those that need to occur first) are photoionizations:

$$O_2 + h\nu \rightarrow O_2^+ + e^- \quad \text{photoionization} \quad \lambda < 102.6\ \text{nm} \tag{11.7a}$$

$$O + h\nu \rightarrow O^+ + e^- \quad \text{photoionization} \quad \lambda < 91.0\ \text{nm} \tag{11.7b}$$

$$N_2 + h\nu \rightarrow N_2^+ + e^- \quad \text{photoionization} \quad \lambda < 79.6\ \text{nm} \tag{11.7c}$$

B. The secondary reactions are as follows:

$$N_2^+ + O \rightarrow N_2 + O_2^+ \qquad \text{charge transfer} \tag{11.3a}$$

$$N_2^+ + O \rightarrow N + NO^+ \qquad \text{ion exchange} \tag{11.3b}$$

$$N_2 + O_2^+ \rightarrow NO + NO^+ \qquad \text{ion/atom exchange} \tag{11.8}$$

As in the F layer, the secondary reactions remove most of the N^+ in favor of O_2^+ and NO^+.

11.1.2.3 Loss Mechanisms

The loss mechanisms for ions of the E layer are

$$O_2^+ + NO \rightarrow O_2 + NO^+ \qquad \text{ion exchange} \tag{11.9}$$

$$NO^+ + e^- \rightarrow N + O \qquad \text{dissociative recombination} \qquad (11.4b)$$

(11.4b) is the most important charge neutralization step in the E layer. Also, (11.9) is much more important than (11.4b) in the E layer because the concentration of neutral NO is much greater than the concentration of free electrons.

The E layer is in photochemical equilibrium during daytime, with diffusion and other motions also becoming important at night.

11.1.3 The D Layer

The D layer is shielded by the E and F layers above it. Most of the ionizing radiation has been absorbed by photodissociation and photoionization of O_2 in the E and F layers; particularly

$$122 \text{ nm} < \lambda < 180 \text{ nm} : O_2 + h\nu \rightarrow O + O \quad \text{photodissociation} \qquad (11.1)$$

$$\lambda < 102.6 \text{ nm} : O_2 + h\nu \rightarrow O_2^+ + e^- \quad \text{photoionization} \qquad (11.7a)$$

11.1.3.1 Dominant Ions

The dominant ions in the D layer are NO^+ (~80 % by number) and O_2 (~20 % by number), plus small but important amounts of other positive and negative molecular ions.

Ionization in the D region comes mainly from four sources:

1. "Windows" in the range 102.6 nm $< \lambda <$ 122 nm, in which radiation reaches down to as low as 70 km. These windows include the Lyman-alpha (Lyα) emission line at $\lambda = 121.6$ nm.
2. Solar X rays in the upper D region, from the quiet (undisturbed) Sun.
3. Cosmic rays in the lower D region. Cosmic rays are particles (electrons, protons, etc.) arriving at the Earth from the Sun (solar cosmic rays) and sources beyond the solar system (galactic cosmic rays). Most of the electrons are stopped by collisions higher in the atmosphere, but energetic auroral electrons can reach the D region, e.g., during magnetospheric substorms (Sect. 11.6.8). Solar energetic protons, which have typical energies in the 100 s of MeV, can penetrate to the D region at high latitudes.
4. Solar X rays of $\lambda < 0.6$ nm during disturbed conditions, especially from solar flares.

11.1.3.2 Production Mechanisms

Production (source) of ions in the D layer is through

A. Primary reactions, which produce mainly NO^+, O_2^+, and O_2^-.

$$NO + h\nu \rightarrow NO^+ + e^- \quad \text{photoionization} \quad \lambda < 134.1 \text{ nm} \tag{11.10a}$$

(Ionization of NO by Lyα photons is the main reason for the existence of the D layer.)

Negative ions also form, by electron attachment in a three-body collision:

$$O_2 + e^- + M \rightarrow O_2^- + M \quad \text{electron attachment} \tag{11.10b}$$

where M is any molecule or atom. Simple attachment, viz., $O_2 + e^- \rightarrow O_2^-$, cannot occur because the reaction $O_2 + e^-$ is exothermic, and the excess energy ejects the electron again unless a third body carries off the energy excess. The third body also allows both energy and momentum to be conserved. Radiative recombination ($O_2 + e^- \rightarrow O_2^- + h\nu$) is too slow to be important.

Negative ions are important only in the D region, because the probability of three-body collisions depends strongly on the density. In the E and F regions, the density is so low that three-body collisions are extremely rare, and negative ions are essentially absent.

B. Secondary reactions:
NO^+, O_2^+ and O_2^- react with a large variety of neutral molecules. As a result, the D layer is a complex system of many ionic species, such as H_3O^+ and O_2^+, and NO_3^-, as well as "cluster ions," such as $H_3O^+ \cdot H_2O$ and $NO_3^-(H_2O)_n$ (where the subscript n is a small integer) that form when neutral molecules become attached to an ionized molecule.

11.1.3.3 Loss Mechanisms

The loss of ions in the D layer is primarily through dissociative recombinations.

Production and loss in the D layer occur much faster than mixing or diffusion. The concentration of each ion at each altitude in the D region is therefore controlled by photochemical equilibrium.

An important consequence of this photochemical equilibrium is that, with the rapidity of loss processes and the removal of solar ionizing radiation, the D layer disappears at night.

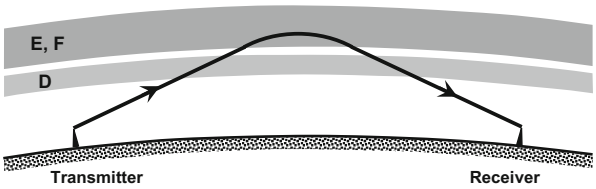

Fig. 11.2 Illustration of the refraction of radio waves by the Earth's ionospheric E and F layers. The diagram is a composite of two scenarios: during the daytime, the waves are absorbed in the D layer and do not reach the receiving antenna, whereas at night the D layer disappears and long-distance reception occurs

11.1.4 Reflection of Radio Waves

The E and F layers permit long-distance radio communication by reflecting radio waves back to the Earth, particularly in the standard commercial AM broadcast band (approximately 500–1,700 kHz) and short wave regions.

Radio waves are emitted by oscillating electric currents in the transmitting antenna. The inverse process takes place in reception: the incoming radio wave creates an oscillating electric current in the receiving antenna.

A similar process happens in the ionosphere. An incoming radio wave encountering a free electron makes the electron oscillate. The oscillating electron in turn behaves as a small transmitting antenna and emits a radio wave of the same frequency as the incoming wave. Each free electron therefore acts as a combination receiver and re-transmitter.

The overall process is complex (see Sect. 11.4), but the result is that the path of the radio wave is bent back toward the Earth; that is, the wave is "reflected" by the ionosphere, as Fig. 11.2 illustrates.

To be reflected by the E and F layers, however, radio waves have to pass twice through the D layer: once on the way up and once on the way back down.

The density in the D layer is high enough that the oscillating electrons collide with the surrounding molecules, removing energy from the electrons and increasing the random motion of the molecules. The electrons as a result are unable to retransmit efficiently, reducing the intensity of the radio beam. Thus, energy is taken from the radio waves and converted to heat in the D layer, with the result that the radio waves are absorbed rather than reflected.

During daytime, the D layer limits the commercial AM band to line-of-sight distances. At night, however, the D layer disappears, allowing long-distance reception.

Intense solar flares produce very energetic particles, which can reach the Earth within half an hour after the start of the flare and can penetrate to the D layer. The enhanced ionization in the D layer can then produce radio blackouts by disrupting long-distance radio communication.

11.2 Atmospheric and Ionospheric Chemistry on Mars and Venus

11.2.1 Neutral Atmosphere of Mars

The mixing ratios[2] of H, H_2, O, O_2, CO, and CO_2 in the Martian atmosphere are shown as a function of altitude in Fig. 11.3. Some of these are also listed in Table 11.1, for the lower atmosphere. The dominant component at all altitudes below 200 km is CO_2, with a mixing ratio of 0.953 in the troposphere.

Because of the thinness of the Martian atmosphere, solar UV penetrates to the ground, and the chemistry of the neutral atmosphere is therefore dominated by photodissociation (photolysis) of CO_2, producing atomic oxygen:

$$CO_2 + h\nu \rightarrow CO + O \quad \text{photodissociation} \quad \lambda < 204\ \text{nm} \tag{11.11}$$

However, as Fig. 11.3 shows, molecular O_2 is much more abundant than atomic O below 100 km altitude. The O_2 is created by OH radicals derived from water, such as OH (hydroxyl) from

$$H_2O + h\nu \rightarrow OH + H \quad \text{photodissociation} \tag{11.12a}$$

$$H_2O + O^* \rightarrow OH + OH \tag{11.12b}$$

[where the superscript (*) signifies an excited state] reacting with atomic oxygen:

$$O + OH \rightarrow O_2 + H \tag{11.13}$$

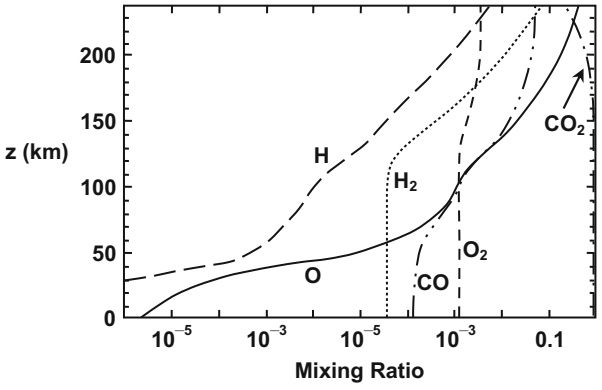

Fig. 11.3 Mixing ratios of H, H_2, O, O_2, CO, and CO_2 in the Martian atmosphere, as a function of altitude, z. Adapted from Nair et al. 1994, Fig. 3(a), p. 133, with permission

[2] Mixing ratio is defined in Footnote 3, Sect. 10.2.2.

Table 11.1 Comparison of the number densities of neutrals and ions in the Martian ionosphere (~130 km altitude)

	Number density (cm^{-3})	
Species	Neutral (CO_2, O_2)	Ion (CO_2^+,O_2^+)
CO_2	4×10^{10}	1.5×10^4
O_2	5×10^7	10^5

Without an opposing oxidizing process to convert CO back to CO_2, (11.11) and (11.13) would produce the observed CO abundance in less than 3 years, and a mostly CO and O_2 atmosphere in about 2,000 years. Figure 11.3 shows that this has not happened. The oxidizing process cannot be direct recombination with O, either by

$$CO + O \rightarrow CO_2^* \rightarrow CO_2 + h\nu \tag{11.14a}$$

or by

$$CO + O + M \rightarrow CO_2 + M \tag{11.14b}$$

because radiative de-excitation of CO_2^+ is too slow to compete with (11.11), and (11.14b) is spin-forbidden. However, Mars has significant quantities of water. Various chemical reactions produce OH (hydroxyl) from water, including (11.12a) and (11.12b). The OH then reacts with CO rapidly enough to compete with CO_2 photolysis:

$$CO + OH \rightarrow CO_2 + H \tag{11.15}$$

11.2.2 Neutral Atmosphere of Venus

Venus' clouds shield the regions below them from solar UV radiation, so photochemistry occurs at and above the cloud tops.

The major steps are similar to those on Mars, specifically,

$$\text{Formation of } O_2: \quad O + O + M \rightarrow O_2 + M \tag{11.16}$$

$$\text{Oxidation of CO}: \quad CO + O \rightarrow CO_2 \quad (\text{net reaction}) \tag{11.17}$$

Reaction (11.16) replaces (11.13) because Venus lacks significant water.

Reaction (11.17) is required because, in similar fashion to Mars, (11.11) and (11.16) would produce the observed O_2 abundance in only a few years and the observed CO abundance in about 200 years. The result should be a mostly CO and O_2 atmosphere from the cloud tops upward. This is true for the highest levels of Venus' atmosphere, but near the cloud tops the concentrations of CO and O_2 are only 45 and 1 ppm, respectively.

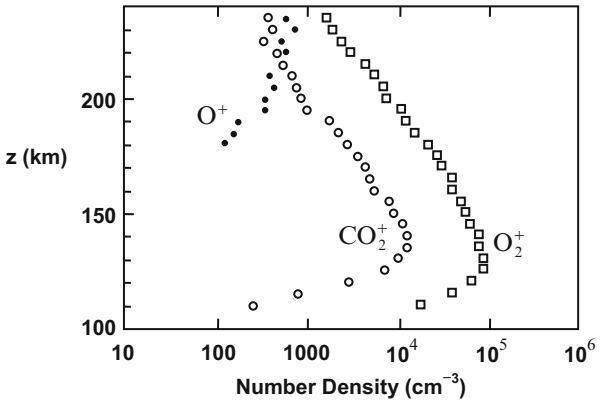

Fig. 11.4 Ion density profiles in the Martian ionosphere. *Open squares* are O_2^+; *open circles* are CO_2^+; and *dots* are O^+. Because each ion contributes one free electron, the electron density is slightly greater than the density of O_2^+. After Chen et al. (1978), Fig. 6, p. 3875); copyright 1978, American Geophysical Union. Modified by permission of American Geophysical Union

Venus differs from Mars in that the CO:O_2 ratio is about 45:1 on Venus, compared to about 1:10 on Mars (Fig. 11.3). Thus, an efficient reaction is needed on Venus to break the O–O bond of O_2. The solution is not clear, but several reaction cycles involving chlorine and/or sulfur appear likely.

11.2.3 Ionosphere of Mars

11.2.3.1 Dominant Ions

The dominant ion in the Martian ionosphere is O_2^+, with smaller amounts of CO_2^+ and O^+ (Fig. 11.4).

It should be noted that, even in the region of greatest ion density (~130 km altitude), ions are a very small minority of the particles present. A similar situation applies to the ionospheres of the Earth and Venus. Table 11.1 lists some representative values.

11.2.3.2 Production Mechanisms

Production is due to the reactions

$$CO_2 + h\nu \rightarrow CO_2^+ + e^- \qquad \text{photoionization } \lambda < 93 \text{ nm} \qquad (11.18)$$

$$CO_2^+ + O \rightarrow O_2^+ + CO \qquad \text{ion exchange} \qquad (11.19a)$$

$$CO_2^+ + O \rightarrow O^+ + CO_2 \qquad \text{charge transfer} \qquad (11.19b)$$

$$O^+ + CO_2 \rightarrow O_2^+ + CO \qquad \text{atomic exchange} \qquad (11.20)$$

Not surprisingly, the primary ionospheric reaction is photoionization of CO_2. However, CO_2^+ is not the dominant ion (Fig. 11.4), because (11.19a) and (11.19b) convert most of the CO_2^+ to O^+ and O_2^+, and (11.20) then converts most of the O^+ to O_2^+.

11.2.3.3 Loss Mechanisms

The most important charge-neutralization reaction is dissociative recombination of the domination:

$$O_2^+ + e^- \rightarrow O + O^* \qquad \text{dissociative recombination} \qquad (11.21)$$

11.2.4 Ionosphere of Venus

11.2.4.1 Dominant Ions

The dominant ions in the ionosphere of Venus are different at different altitudes, as on Earth:

Low altitudes (110–200 km): O_2^+ and NO^+
High altitudes (>200 km): O^+
Other ions present include C^+, CO^+, CO_2^+, N^+, N_2^+, H^+, He^+.

Below 170 km, the ionosphere is in photochemical equilibrium, i.e., abundances are determined by local production and loss. Above 170 km, abundances are determined primarily by diffusion.

11.2.4.2 Production and Loss Mechanisms

Reactions (11.18)–(11.20) apply on Venus as on Mars. In addition, one of the loss reactions for O_2^+ is the major source for NO^+:

$$O_2^+ + N \rightarrow NO^+ + O \quad \text{ion exchange} \qquad (11.22)$$

The NO^+ also contributes to the production neutral O:

$$NO^+ + e^- \rightarrow N + O \quad \text{dissociative recombination} \qquad (11.4b)$$

Production of O^+ is by

$$O + h\nu \rightarrow O^+ + e^- \quad \text{photoionization } \lambda < 91.0 \text{ nm} \tag{11.2a}$$

$$O + e^- \rightarrow O^+ + 2e^- \quad \text{electron impact} \tag{11.23}$$

$$CO_2^+ + O \rightarrow O^+ + CO_2 \quad \text{charge transfer} \tag{11.19b}$$

Loss of O^+ is by

$$O^+ + NO \rightarrow NO^+ + O \quad \text{charge transfer} \tag{11.24a}$$

$$O^+ + CO_2 \rightarrow O_2^+ + CO \quad \text{atomic exchange} \tag{11.20}$$

$$O^+ + H \rightarrow H^+ + O \quad \text{charge transfer} \tag{11.24b}$$

Reactions (11.19b) and (11.20) emphasize the importance of CO_2 on Venus.

11.2.5 Atmospheric Escape Mechanisms

11.2.5.1 Jeans Escape

The particles (atoms or molecules) of a gas in thermal equilibrium (in which case the gas has a well-defined temperature, T) are said to have a thermal, or *Maxwellian*, distribution of speeds. At and above the exobase (the base of the exosphere, Sect. 10.4.1.4), those particles in the Maxwellian distribution that are travelling upward with speeds above escape speed, v_{esc}, will escape. This type of atmospheric loss is called *Jeans escape*, and gives rise to the evaporation phenomenon discussed in connection with long-term retention in Sect. 10.1.

The flux of escaping particles (m^{-2} s^{-1}) is given by

$$\Phi_J = n_x \frac{v_{th}}{2\sqrt{\pi}} P_{esc} = n_x \frac{v_0}{4} P_{esc} \tag{11.25}$$

(e.g., Hunten 1982, and references therein), where a subscript "x" signifies a value at the exobase, $v_{th} = \sqrt{2kT_x/m}$ is the most probable particle speed, $v_0 = \sqrt{8kT_x/(\pi m)}$ is the mean of the magnitudes of the particle speeds, k is Boltzmann's constant, T_x and n_x are the temperature and particle density (m^{-3}), respectively, at the exobase (the exosphere is isothermal, whereas density decreases with altitude), m is the mass per particle, $P_{esc} = (1 + \lambda_J) \exp(-\lambda_J)$ is the probability of escape, λ_J is the *Jeans parameter*, equal to the magnitude of the ratio of the gravitational energy, $E_{grav} = GMm/r$, of a particle to its thermal energy, $E_{th} = kT$, at the exobase,

$$\lambda_J \equiv \left|\frac{E_{grav}}{E_{th}}\right| = \frac{GMm}{kT_x r_x} = \frac{r_x}{H_x} = \left(\frac{v_{esc}}{v_{th}}\right)^2 \tag{11.26}$$

(see Problem 1 in the Challenges section at the end of this chapter), G is the universal gravitational constant, M is the planetary mass, r_x is the radial distance of the exobase from planetary center, $H_x = kT_x/(mg)$ is the pressure scale height at the exobase [cf. (10.26)], and g is the gravitational acceleration at the exobase. A correction factor, B ($0.5 \leq B \leq 0.8$), is sometimes included in (11.25) to allow for the depression of the high-velocity tail of the Maxwellian distribution by the escape of high-velocity particles (Hunten 1982).

The quantities v_{th}, v_o and P_{esc}, and therefore also Φ_J, all decrease with increasing particle mass, m. ($\lambda_J \propto m$ but, for large λ_J, the value of P_{esc} is dominated by the $\exp(-\lambda_J)$ factor.) Thus, for a given element, Jeans escape results in isotope fractionation: lighter isotopes become increasingly depleted as a function of time relative to heavier isotopes. Nonthermal loss mechanisms (Sect. 11.2.5.3) also contribute, and can in fact dominate, isotope fractionation. This effect makes isotope ratios a useful probe for investigating atmospheric history.

Another useful relation can be found from the fact that the mean free path, L_{mfp}, equals the total density scale height (i.e., including all species), H_{total}, at the exobase. H_{total} is related to the total number density (all species), n_{total}, and the mean collisional cross section, σ, by $L_{mfp} = 1/(n_{total}\sigma)$. It then follows that, at the exobase,

$$n_{x,total}\, H_{x,total}\, \sigma = 1 \tag{11.27}$$

On Venus, the exobase altitude is ~200 km, where the dominant species is atomic oxygen, followed by CO and then several other species including atomic hydrogen. Because of its large scale height, H becomes the major species after O at higher levels in the exosphere. The temperature is 275 K in the dayside thermosphere and 100 K in the nightside cryosphere. Number densities vary over the solar cycle; taking a number density for hydrogen of $n_x \sim 6 \times 10^{10}$ m^{-3}, (11.25) and (11.26) give, for H in the dayside exosphere, $\lambda_J = 22.87$, $P_{esc} = 2.8 \times 10^{-9}$, $\Phi_J = 1.0 \times 10^5$ m^{-2} s^{-1}, and a total loss rate of H from the dayside exosphere by Jeans escape of $2\pi\, r_x^2 \Phi_J = 2.5 \times 10^{19}$ s^{-1}.

As noted above, loss rates decrease strongly with increasing λ_J when λ_J is large. On the dayside, (11.26) gives $\lambda_J = 46$ for deuterium and 366 for atomic O, and on the nightside, $\lambda_J = 66.88$ for atomic hydrogen (giving a nightside hydrogen loss rate $<10^4$ s^{-1}). Thus, Jeans escape on Venus is by far dominated by H atoms from the dayside exosphere.

In the case of Mars, there is considerable uncertainty in the temperature and hydrogen density at the exobase (e.g., Chaufray et al. 2008). From *Mars Express* observations of Lyman α scattering by the hydrogen corona, Chaufray et al. (2008) use radiative transfer models to derive the H density profile and temperature (isothermal) in the exosphere, and, from that, the temperature and H density at

the exobase (200 km altitude). Assuming that exospheric H is characterized by a single temperature, they obtain $T_x = 200$–250 K and a hydrogen number density $n_x \sim 1$–4×10^{11} m^{-3}. Using $T_x = 225$ K and $n_x \sim 2.1 \times 10^{11}$ m^{-3}, we get $\lambda_J \sim 6.41$, $P_{esc} \sim 1.2 \times 10^{-2}$, and $\Phi_J \sim 1.4 \times 10^{12}$ m^{-2} s^{-1}. Their assumption of spherical symmetry means that T_x is an average over the planet, so the total loss rate of H from the exosphere by Jeans escape is $4\pi r_x^2 \Phi_J \sim 2.2 \times 10^{26}$ s^{-1}. This loss rate is seven orders of magnitude greater than for Venus. The exospheric temperatures of the two planets are reasonably similar, so the difference arises from Venus' greater mass and gravitational acceleration.

As will be seen in Sects. 11.7.2.3 and 11.7.3.2, Jeans escape of H atoms from Venus is negligible compared to other, nonthermal mechanisms, whereas Jeans escape dominates the loss of H from Mars. On both planets, Jeans escape of O, O_2 and CO_2 is negligible.

11.2.5.2 Hydrodynamic Escape

In Jeans escape, atmospheric loss is governed by individual particle motion, and the loss rate can be described by kinetic theory. The rate of Jeans escape decreases with increasing atomic or molecular mass, causing isotope ratios to change.

If the loss rate becomes large enough, the lightest and therefore fastest-moving particles will drag the other particles along with them, and the escape is described by fluid mechanics. This latter condition is called *hydrodynamic escape*, sometimes referred to as *blow-off*. In detail, the lighter particles diffuse through the heavier particles, thus also transferring momentum to them (Hunten et al. 1987). Everything then moves outward, with relative speeds given by diffusion theory. Because all particles flow outward together (or almost together), hydrodynamic escape leaves isotope ratios essentially unchanged.

Jeans escape and hydrodynamic escape can be seen as two end-members of a single atmospheric loss process, with the particular description depending on the relative magnitudes of E_{grav} and E_{th}; i.e., on the value of λ_J. The loss is by Jeans escape for large λ_J and by hydrodynamic escape for small λ_J. Intermediate cases ($\lambda_J \sim 2$) are often called *slow hydrodynamic escape*, and are more difficult to model.

The solar wind (Sect. 11.3) is described by hydrodynamic escape within a few solar radii of the solar photosphere, and the Earth's polar wind (Sect. 11.2.5.3(g), below) can be treated hydrodynamically, but otherwise hydrodynamic escape is not important for planetary atmospheres in the present solar system. However, it may have been important in some cases in the early solar system; e.g., Venus may have had abundant water early in its life, in the form of a primitive atmosphere laden with water vapor because of the high temperature. In this case, photodissociation of H_2O could have led to hydrodynamic escape until the water content dropped below some low level.

Both Jeans escape and hydrodynamic escape are thermal mechanisms. We now turn to nonthermal mechanisms.

11.2.5.3 Nonthermal Loss Mechanisms

Nonthermal processes are those that do not produce a thermal, or Maxwellian, distribution of speeds; e.g., an exothermic chemical reaction may produce atoms or ions with a narrow range of speeds or energies. If these speeds are much higher than the characteristic local thermal (Maxwellian) speed, then they are referred to as *suprathermal* atoms or ions.

Escape requires speeds greater than or equal to v_{esc}: 10–11 km/s for Venus and the Earth, or 5 km/s for Mars. These escape speeds correspond to particle energies of 0.5–0.6 eV per atomic mass unit for Venus and the Earth (1 eV = 1 electronvolt = 1.602×10^{-19} J), or 0.13 eV/u for Mars. If these were mean energies in a thermal distribution, then, by E ~ kT, 0.5 eV/u would correspond to a temperature increment of ~6,000 K for each atomic mass unit; i.e., characteristic temperatures of 6,000 K × 1 for H and 6,000 K × 16 = 96,000 K for O, much higher than the actual exospheric temperatures of ~300 K for Venus or 1,000 K for the Earth. Similarly, 0.13 eV/u corresponds to ~1,500 K for H or 24,000 K for O, compared to the Martian exospheric temperature of ~200 K. Nonthermal processes therefore have to create significant quantities of suprathermal atoms/ions to influence atmospheric loss.

Not all suprathermal atoms have sufficient energy to escape. Because of their high energies, they have a very large scale height and create a high-altitude corona around the planet. "Hot" (i.e., high-energy) H and O coronae have been observed around Venus, the Earth, and Mars.

The important nonthermal loss mechanisms are listed below (Hunten 1982). In this list, an asterisk denotes a high kinetic energy.

a. Charge exchange:

$$\text{e.g.,} \quad H^{+*} + H \rightarrow H^{*} + H^{+} \tag{11.28}$$

$$H^{+*} + O \rightarrow H^{*} + O^{+} \tag{11.29}$$

$$D^{+*} + H \rightarrow D^{*} + H^{+} \tag{11.30}$$

Ions are constrained by the magnetic field of the planet, whereas neutrals are not. Charge exchange therefore converts fast ions which cannot escape into fast neutrals which can, while the thermal neutral is converted into a thermal ion. The fast neutrals that do not escape help populate the hot H and O coronae.

(11.28) is the dominant loss mechanism for the Earth: Characteristic temperatures for plasmaspheric and ionospheric protons and deuterons are ~2,000–10,000 K, compared ~750–1,750 K for exospheric neutrals.

b. Dissociative recombination:

$$\text{e.g.,} \quad O_2^{+} + e^{-} \rightarrow O^{*} + O^{*} \text{ (energy divided equally)} \tag{11.21}$$

$$OH^{+} + e^{-} \rightarrow O + H^{*} \text{ (H takes almost all of the energy)} \tag{11.31}$$

(11.21) releases 2.5 eV of kinetic energy to each oxygen atom; then, by (10.2), each oxygen atom has a speed $v = 5.5$ km/s, equal to the escape speed from Mars. Oxygen is abundant in terrestrial planet exospheres, so (11.21) is an important source of energetic atomic oxygen on Earth, Venus and Mars. It also indirectly produces energetic H and D by elastic energy transfer collisions [(11.36)].

c. Impact dissociation and photodissociation:

$$\text{e.g.,} \; N_2 + e^{-*} \rightarrow N^* + \; N^* \tag{11.32}$$

$$O_2^* + h\nu \rightarrow O^* + \; O^* \tag{11.33}$$

The e may be a photoelectron or an accelerated electron. In this and the previous mechanism, it is also possible for much of the photon or electron energy to go into electronic or vibrational excited states of the product atoms or molecules, reducing the kinetic energy available for escape. These H*, N* and O* would then contribute to their respective coronae.

d. Ion-neutral reaction:

$$\text{e.g.,} \quad O^+ + H_2 \rightarrow OH^+ + H^* \tag{11.34}$$

(11.34) yields 0.6 eV, but much of this energy is likely to go into vibrational excitation of the OH. In this case, most of the H will enter the H corona rather than escaping.

e. Sputtering and knock-on:

$$\text{e.g.,} \quad Na + S^{+*} \rightarrow Na^* + \; S^{+*} \; \text{Sputtering (requires keV or greater)} \tag{11.35}$$

$$O^* + \; H \rightarrow O^* + \; H^* \qquad \text{Knock−on (elastic energy transfer)} \tag{11.36}$$

Sputtering refers to a backsplash of atoms caused by the impact of an energetic incident particle. It is usually thought of in terms of impacts on solid surfaces, such as sputtering of atoms and ions from the lunar surface by impacting solar wind particles, but also occurs with particles striking planetary atmospheres. In this case, multiple secondary collisions result in some particles travelling backward. Knock-on refers to forward acceleration of impacted particles.

Incident ions are usually the agents of sputtering, but only because the required speeds are seldom achieved by neutral atoms.

f. Solar wind pickup:

$$\text{e.g.,} \quad O + h\nu \rightarrow O^+ + e^- \; \text{(or ionization by electron impact)} \tag{11.37}$$

A neutral planetary corona can extend beyond the planetary magnetosphere into the solar wind, because neutral atoms are not constrained by magnetic fields. If such an atom is ionized as described above, then it suddenly finds itself as a charged particle in a moving magnetic field (the interplanetary magnetic field embedded in the solar wind). It therefore experiences a motional electric field that causes it to drift at the solar wind speed in the solar wind direction (see Sect. 11.5.6); i.e., it is picked up and carried off by the solar wind. These ions are referred to as *pickup ions*.

This loss mechanism also occurs on satellites in a planetary magnetospheric wind.

g. Ion escape:

e.g., escape of H^{+}* along open magnetic field lines. This process is important in the Earth's polar regions, where the magnetic field lines are open to the magnetotail (Sect. 11.5). The flux of ions is called the *polar wind*.

h. Plasma waves:

At high altitudes where the density is low enough for the plasma to be essentially collisionless, plasma waves involving broad-band, low-frequency electric-field oscillations in the range <1 Hz to several hundred Hz can accelerate ions to energies of tens to hundreds of eV, and even up to several keV (André and Yau 1997). A collisionless plasma is required to avoid losses by collisions and charge exchange. Several types of interactions can occur; e.g., resonant energy transfer from the waves to the ions when the plasma wave frequency is close to the gyrofrequency of the ions. The average global escape rate at Earth is ~1 kg/s (Knudsen 2013, *personal communication*).

Plasma wave acceleration is important in the dayside polar cusp (Fig. 11.23), creating a feature known as the cusp ion fountain that spews ions of all masses into the magnetosphere, and similar heating takes place on the night side, particularly near the poleward boundary of the auroral oval (Knudsen 2013, *personal communication*).

11.3 Solar Wind

The solar wind is composed of charged particles (electrons and positive ions) streaming out from the Sun. More than 99 % of the ions are H^{+} and $^{4}He^{2+}$, and the rest are $^{3}He^{2+}$, C, O, and other ions. Of the H^{+} and $^{4}He^{2+}$, 95–96 % is H and 3.5–4.5 % is He.

The solar wind behaves as a highly conducting medium, so the relative numbers of electrons and ions maintain charge neutrality.

There is a region of acceleration close to the Sun where the particles are accelerated from low speeds to about 400 km/s (Table 11.2). Thereafter, the speed is approximately constant.

Table 11.2 Typical solar wind values

r	$1.03R$	$1.5R$	$10R$	1 AU
n_{ion} (m^{-3})	2×10^{11}	1×10^{11}	2×10^{9}	5×10^{6}
T (K)	1.7×10^{6}	10^{6}	4×10^{5}	4×10^{4}
B (T)	10^{-4}	5×10^{-5}	10^{-6}	4×10^{-9}
v (km/s)	0.6	3	300	400

For uniform expansion at constant speed, the number density of particles will decrease as one over the surface area, i.e., $n \, \alpha \, r^{-2}$. In particular, if r is the distance from the Sun in AU, then the number density of ions is given by

$$n_{\text{ion}}\left(\text{m}^{-3}\right) = \frac{5 \times 10^{6}}{r^{2}(\text{AU})} \tag{11.38}$$

Variations in these values are produced by high-speed jets (~600 km/s) of steady flow from coronal holes and by transient events including ejections by eruptive prominences, solar flares, and other active phenomena on the Sun.

The solar wind can be detected at great distances from the Sun, as discovered by *Voyager* I, which has just reached the region of sharply decreased solar wind, the edge of the heliosphere, ~126 au from the Sun.

11.4 Maxwell's Equations and the Plasma Frequency

A *plasma* is an ionized medium consisting of ions and free electrons. If in a plasma the charges of one sign are displaced relative to those of the other sign, creating a charge separation, the restoring force causes the charges to oscillate relative to each other at the *plasma frequency*, f_0. The behavior of electromagnetic waves traveling through a plasma depends on how the frequency, f, of the waves relates to f_0. We will now examine this dependence, making use of Maxwell's powerful formulation of electromagnetism.

11.4.1 Maxwell's Equations

Two of Maxwell's equations for free space may be written as follows (Griffiths 1999, p. 130):

$$\dot{\mathbf{B}} = -\vec{\nabla} \times \mathbf{E} \tag{11.39}$$

$$\dot{\mathbf{D}} + \mathbf{J} = -\vec{\nabla} \times \mathbf{H} \tag{11.40}$$

where

$$\mathbf{B} = \mu_o \mathbf{H} \tag{11.41}$$

$$\mathbf{D} = \varepsilon_0 \mathbf{E} \tag{11.42}$$

$$\mathbf{J} = \sum_k N_k q_k \mathbf{v}_k \tag{11.43}$$

In (11.43), the summation is over all species of charge carriers (electrons and each type of ion), N_k is the number density of the kth species, q_k is the charge (with sign) of the kth species, and $\mathbf{v}_k$ is the mean or drift velocity of the kth species. In this section, we use N in order to reserve n for the refractive index.

Other symbols are

$\mathbf{B}$ = magnetic flux density, unit: tesla[3] (1 T = 1 Wb/m^2 = 1 kg s^{-2}A^{-1});
$\mathbf{E}$ = electric field strength or electric intensity,
unit: N/C = V/m = m kg s^{-3}A^{-1};
$\mathbf{H}$ = magnetic field strength, unit: A/m;
$\mathbf{D}$ = electric displacement, unit: C/m^2;
$\mathbf{J}$ = current density, unit: A/m^2;
e = magnitude of the charge on the electron = 1.602177×10^{-19} C;
ε_0 = permittivity of free space = 8.85×10^{-12} F/m;
μ_0 = permeability of free space = $4n \times 10^{-7}$ N/A^2;
$\vec{\nabla}$ = gradient or del operator, $\vec{\nabla} \equiv \frac{\partial}{\partial x}\hat{\mathbf{i}} + \frac{\partial}{\partial y}\hat{\mathbf{j}} + \frac{\partial}{\partial z}\hat{\mathbf{k}}$.

Our task will be to obtain from (11.39) to (11.43) an equation involving only the electric field and its derivatives and to use this equation to study the interaction of the electric vector of a wave with an ionized medium. In particular, we will consider a medium that is charge-neutral, and $\mathbf{J}$ is dominated by a single species of charge carrier of charge q. In this case, (11.43) can be replaced with:

$$\mathbf{J} = Nq\mathbf{v} \tag{11.43a}$$

The result will, for example, be applicable to the ionosphere, where the mobility of electrons is much greater than that of the ions. In this case, $q = -e$ is the charge on an electron, and $\mathbf{v}$ is in the direction of motion of the electrons.

Step 1: Take the curl[4] of (11.39) and the time derivative of (11.41), and substitute the latter into the former to obtain

[3] The SI unit of magnetic flux is the weber: 1 Wb = 1 weber = 1 T m^2. B is therefore the magnetic flux density; i.e., the magnetic flux per unit area: 1 T = 1 Wb/m^2.

[4] The curl of any vector field, $\vec{F}$, written $\vec{\nabla} \times \vec{F}$, is a measure of rotation in the field. [A vector field is a representation of a vector quantity that (in general) has a different magnitude and direction at each point in space; e.g., the magnetic flux density, $\vec{B}$]. An intuitive way to think of curl is to imagine the vector field as representing flow vectors in a fluid. If a little paddlewheel placed at some point rotates as the fluid flows past it, then the vector field has non-zero curl at that point.

$$\mu_0 \vec{\nabla} \times \dot{\mathbf{H}} = -\vec{\nabla} \times \vec{\nabla} \times \mathbf{E} \tag{11.44}$$

Step 2: Substitute (11.43a) into (11.40), and take the time derivative of (11.42) to eliminate $\dot{\boldsymbol{D}}$ to obtain

$$\varepsilon_0 \dot{\mathbf{E}} + Nq\mathbf{v} = \vec{\nabla} \times \mathbf{H} \tag{11.45}$$

Step 3: Differentiate (11.45) and multiply through by μ_0 to get

$$\mu_0 \varepsilon_0 \ddot{\mathbf{E}} + \mu_0 Nq\dot{\mathbf{v}} = \mu_0 \vec{\nabla} \times \dot{\mathbf{H}} \tag{11.46}$$

Step 4: Substitute (11.44) into the right-hand side of (11.46) to obtain

$$\mu_0 \varepsilon_0 \ddot{\mathbf{E}} + \mu_0 Nq\dot{\mathbf{v}} = -\vec{\nabla} \times \vec{\nabla} \times \mathbf{E} \tag{11.47}$$

Step 5: Use the identity

$$-\vec{\nabla} \times \vec{\nabla} \times \mathbf{E} = \nabla^2 \mathbf{E} + \vec{\nabla}\left(\vec{\nabla} \bullet \mathbf{E}\right) \tag{11.48}$$

to obtain

$$\mu_0 \varepsilon_0 \ddot{\mathbf{E}} + \mu_0 Nq\dot{\mathbf{v}} = \nabla^2 \mathbf{E} + \vec{\nabla}\left(\vec{\nabla} \bullet \mathbf{E}\right) \tag{11.49}$$

Generally, the *divergence* of $\mathbf{E}$ is $\vec{\nabla} \bullet \mathbf{E} = Q/\varepsilon_0$ (*Gauss's law*), where Q is the net charge. In the case of multiple charge species, $Q = \sum_k N_k q_k$. For charge neutrality, $\vec{\nabla} \bullet \mathbf{E} = 0$.

The electron current is produced by the $\mathbf{E}$ field initially, therefore the force is electrostatic, and Newton's second law ($\sum \mathbf{F} = m\mathbf{a}$) gives

$$q\mathbf{E} = m\dot{\mathbf{v}} \tag{11.50}$$

where $m = 9.10838 \times 10^{-31}$ kg is the mass of the electron. Whence,
Step 6: Substitute (11.50) into (11.49) to obtain

$$\mu_0 \varepsilon_0 \ddot{\mathbf{E}} + \mu_0 \frac{Ne^2}{m} \mathbf{E} = \nabla^2 \mathbf{E} \tag{11.51}$$

where we have used $q = -e$. Now we are in a position to apply Maxwell's equations to a radio wave passing through the ionosphere.

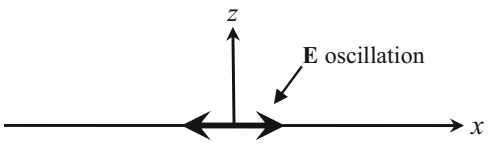

Fig. 11.5 A polarized electromagnetic wave traveling in the z-direction, with its electric field oscillation in the x-direction

11.4.2 Application to a Polarized Wave

Assume now that a polarized wave ascends vertically (in the z or $\hat{\mathbf{k}}$ unit vector direction), with the **E**-field polarized in the x or $\hat{\mathbf{i}}$ direction, as illustrated in Fig. 11.5.

Adopt a trial solution to (11.51) of the form

$$\mathbf{E} = \mathrm{E}_x\hat{\mathbf{i}} = \mathrm{E}_0 \exp\left[\mathrm{j}\omega\left(t - \frac{nz}{c}\right)\right]\hat{\mathbf{i}} \tag{11.52}$$

where $\mathrm{j} = \sqrt{-1}$ and $n = c/v$ is the index of refraction. The last term in (11.52) is equal to

$$\left(\frac{n}{c}\right)\omega z = 2\pi f\left(\frac{n}{c}\right)z = 2\pi f\,\frac{z}{v} = 2\pi\frac{z}{\lambda} \tag{11.53}$$

where we make use of the relation $v = f\lambda$.

Insert (11.52) into (11.51) and define $\alpha \equiv j\omega\,(t - nz/c)$ to obtain

$$-\mu_0\varepsilon_0\omega^2\mathrm{E}_0\,\exp[\alpha]\hat{\mathbf{i}} + \frac{\mu_0 Ne^2}{m}\mathrm{E}_0\,\exp[\alpha]\hat{\mathbf{i}} = -\frac{\omega^2 n^2}{c^2}\mathrm{E}_0\,\exp[\alpha]\hat{\mathbf{i}}$$

or

$$-\mu_0\varepsilon_0\omega^2 + \frac{\mu_0 Ne^2}{m} = -\frac{\omega^2 n^2}{c^2} \tag{11.54}$$

Solving for n and using $c^2 = 1/(\mu_0\varepsilon_0)$, we obtain the dispersion relation for an ionizing medium:

$$n^2 = 1 - \frac{Ne^2}{m\varepsilon_0\omega^2} \tag{11.55}$$

or, recalling that $\omega = 2\pi f$,

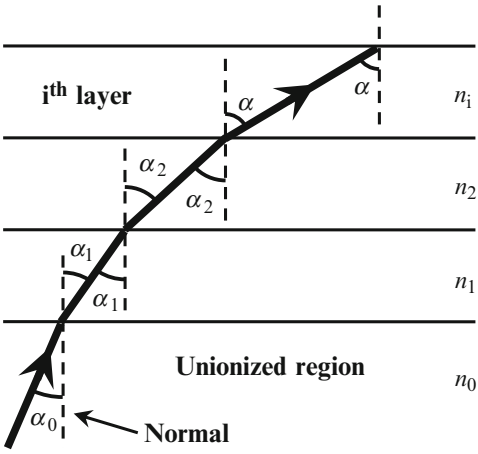

Fig. 11.6 Refraction of an electromagnetic wave in a layered ionosphere of decreasing refractive index, n_i

$$n^2 = 1 - \frac{f_0^2}{f^2} \tag{11.56}$$

where

$$f_0^2 = \left(\frac{1}{2\pi}\right)^2 \left[\frac{Ne^2}{m\varepsilon_0}\right] \tag{11.57}$$

defines the *plasma frequency*, f_0. From (11.56) and (11.57), we have

1. For a vacuum, $f_0 = 0$ and $n = 1$; or, for $N > 0$,
2. n is real and $0 < n < 1$ for $f > f_0$;
3. $n = 0$ for $f = f_0$; and
4. n is imaginary for $f < f_0$.

We now look at some consequences of (11.56) and (11.57) for an electromagnetic wave of frequency f propagating from an unionized region into a region of increasing ionization, e.g., upward into a planetary ionosphere from below or downward from space (cf. Figs. 11.1, 11.2, and 11.4).

In Fig. 11.6, a hypothetical ionosphere is divided into layers of constant electron density, N, with N increasing in successive layers upward from $N_0 = 0$ in the region below the ionosphere. An electromagnetic wave of frequency f in the region below the ionosphere (refractive index n_0) encounters the ionosphere at an incident angle α_0, refracts into the first layer (refractive index n_1) at an angle of refraction α_1, the second layer (refractive index n_2) at angle a_2, and the *ith* layer (refractive index n) at angle α.

Because in (11.57) $f_0 \propto \sqrt{N}$ it follows from (11.57) that $n < 1$ and decreases with increasing N. Thus, n decreases upward in Fig. 11.6 and, from Snell's law [(11.58), below], the wave refracts away from the normal, as shown.

From Snell's law,

$$n_1 \sin\alpha_1 = n_0 \sin\alpha_0 = \text{const} \tag{11.58}$$

$$n_2 \sin\alpha_2 = n_1 \sin\alpha_1 \tag{11.59}$$

Therefore,

$$n_2 \sin\alpha_2 = n_0 \sin\alpha_0 = \text{const} \tag{11.60}$$

Continuing this argument to the *ith* layer and dropping the subscript for the *ith* layer, we get

$$n \sin\alpha = n_0 \sin\alpha_0 = \text{const} \tag{11.61}$$

Thus, as long as the wave is able to reach the ith layer, the angle of refraction there depends only on the refractive indices n_0 and n and the incident angle α_0 and is independent of the characteristics of the ionosphere in the intervening layers. The result is also independent of the thickness of the layers, so we can take the limit as the thickness approaches zero, i.e., (11.61) applies also to continuous media (real ionospheres).

We now note that for a wave entering the ionosphere from space (vacuum), $n_0 = 1$; and for a wave entering from below, the ion density is low enough that n_0 can again be taken as (very close to) 1.

It is apparent from Fig. 11.6 that if α reaches a value $\pi/2$ then the wave can proceed no further and is reflected (internal reflection). Setting $\alpha_{\max} = \pi/2$ and $n_0 = 1$ in (11.61) gives

$$n = \sin\alpha_0 \tag{11.62}$$

i.e., for a given incident angle, the wave will be reflected if the minimum refractive index in the ionosphere is less than $n = \sin\alpha_0$. Define f_0^{peak} to be the maximum plasma frequency in the ionosphere, in the layer of maximum electron density. Then, from (11.56), a wave will be transmitted through the ionosphere only if its frequency exceeds a critical frequency, f_c, given by

$$n^2 = 1 - \frac{\left(f_0^{\text{peak}}\right)^2}{f_c^2} = \sin^2\alpha_0 = 1 - \cos^2\alpha_0 \tag{11.63}$$

or

$$f_c = \frac{f_0^{\text{peak}}}{\cos\alpha_0} = f_0^{\text{peak}} \sec\alpha_0 \tag{11.64}$$

For normal incidence ($\alpha_0 = 0$), $\cos\alpha_0 = \sec\alpha_0 = 1$, so from (11.64)

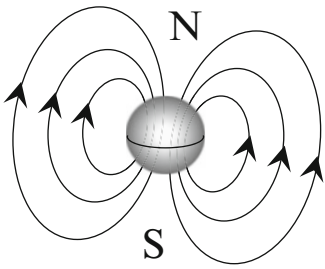

Fig. 11.7 The Earth's intrinsic dipolar magnetic field (Not to scale)

$$f_c = f_0^{\text{peak}} \qquad \text{(normal incidence)} \qquad (11.65)$$

Thus, from (11.56), the wave reflects at the first point (if any) where the refractive index is

$$n = \sqrt{1 - \left(\frac{f_0^{peak}}{f_c}\right)^2} = 0$$

It follows that electromagnetic waves cannot propagate in a region of imaginary refractive index.

11.5 The Earth's Magnetosphere

A planet's magnetosphere is the region of space around the planet occupied by its magnetic field. The magnetosphere constrains the motions of charged particles (electrons and ions) within it, sometimes producing very strong electric fields, electric potential differences, and electric currents and is itself shaped by the charged particles within it and by the solar wind.

We begin with a discussion of the Earth's magnetosphere, as illustrative of processes that take place in planetary magnetospheres in general.

The intrinsic magnetic field of the Earth, created by a self-exciting dynamo in the molten metallic core, is approximately dipolar, as illustrated schematically in Fig. 11.7. The dipole moment is currently 8×10^{22} amp m^2, but varies secularly. The minimum value[5] over the last 3,000 years was 7.7×10^{22} amp m^2 in ~900 AD

[5] The magnetic field configuration at the Earth's surface at earlier times can be determined from archaeomagnetic and paleomagnetic data; e.g., the last time a clay hearth was heated above the Curie point and cooled again, the magnetic orientation of iron in the clay aligned itself with the magnetic field of the Earth at that time and location. Lake sediments have also been used, because iron in the sediments aligns itself with the local magnetic field as the material settles.

and the maximum was 10.4×10^{22} amp m^2 in ~100 BC (Korte and Constable 2011). The magnetic axis is tilted by ~11° relative to the rotation axis and also offset by 515 km radially from the rotation axis toward ~140° E longitude (2009 values, Olson and Deguen 2012) and ~50 km N of the equator, resulting in an offset between the geomagnetic poles and the geographic poles. These values also change secularly. As of the present writing, the north geomagnetic pole is in the Canadian arctic, but wanders with time, and is currently showing signs of migrating to Siberia.

By convention, magnetic field lines point away from a magnetic north (N) pole and toward a magnetic south (S) pole; but also by convention, the geomagnetic poles are labeled according to the geographic hemisphere (N or S) in which they occur. As Fig. 11.7 illustrates, with the magnetic field lines entering the Earth at the North Pole and leaving at the South Pole, these conventions result in the geomagnetic north pole actually being a magnetic south pole and vice versa.

(Historically, the "north" pole of a magnet or compass needle was called the "north-seeking" pole, i.e., the pole that seeks the geographic, or actually geomagnetic, north pole.)

If left to itself, the Earth's dipole field would extend to infinity in all directions. However, the flow of solar wind plasma and *interplanetary magnetic field* (IMF) past the Earth modifies the dipole field as shown in Fig. 11.8.

The *magnetopause* in Fig. 11.8 is the boundary between the Earth's magnetic field and the IMF, i.e., the magnetosphere is the region inside the magnetopause. The solar wind is supersonic, but the solar wind particles are slowed to subsonic speeds by their interaction with the Earth. The *bow shock* marks this transition from supersonic to subsonic flow. Between the bow shock and the magnetopause is a region of subsonic solar wind particles and IMF called the *magnetosheath*. Since disturbances cannot propagate upstream in supersonic flow, the bow shock marks the furthest extent of influence of the Earth's magnetic field.

As is evident in Fig. 11.8, the solar wind substantially compresses the dipole field on the upstream side of the Earth, while on the downstream side, viscous interaction between the solar wind and the magnetospheric plasma stretches the Earth's magnetosphere into a long *magnetotail,* through processes described below. Because of this stretching, magnetic field lines in the magnetotail are approximately parallel to a warped central plane called the *neutral sheet*. Continuity requires that the magnetic field lines above and below join through the neutral sheet; thus, on the neutral sheet the component of magnetic field parallel to the sheet is zero (this characteristic defines the neutral sheet) and the perpendicular component is extremely weak. Therefore, the neutral sheet can be regarded as a plane of essentially zero magnetic field.

The interaction of charged particles in both the magnetospheric plasma and the solar wind with the Earth's magnetic field produces large-scale currents, as illustrated in Fig. 11.9.

We now develop some of the basic physics of the interaction of charged particles with magnetic fields, as it applies to the Earth's magnetosphere in Fig. 11.8 and the currents in Fig. 11.9.

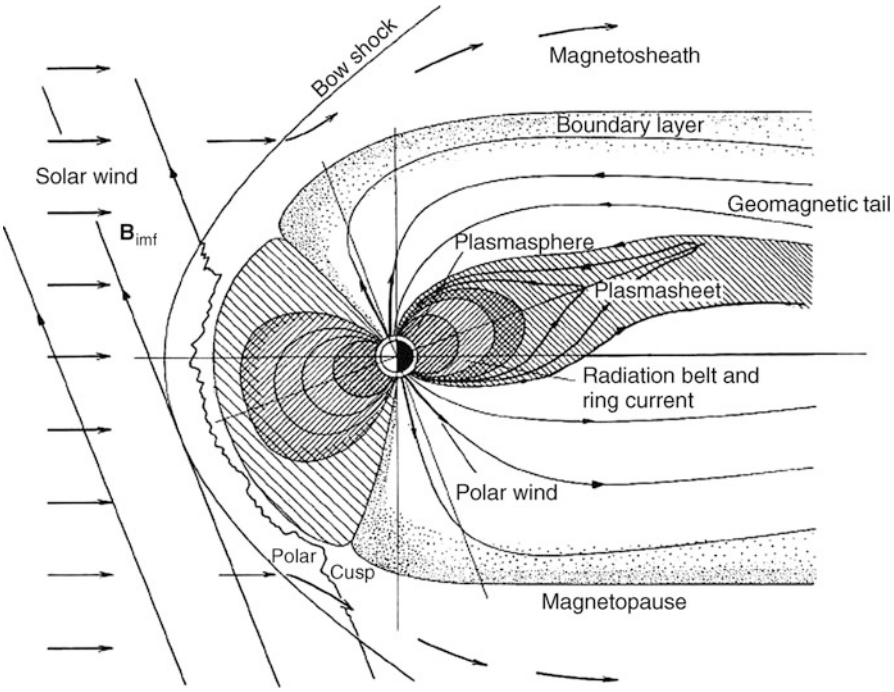

Fig. 11.8 Schematic diagram of the Earth's magnetosphere in the noon-midnight plane. The basic particle and magnetic field features are representative of other internally generated planetary magnetospheres, although the details may be different (from Parks 1991, Fig. 1.3, p. 8, reproduced with the author's permission.)

11.5.1 Forces Acting on Charged Particles

11.5.1.1 The Lorentz Force

The Lorentz force on a charged particle is the vector sum of the electric and magnetic forces:

$$\vec{F} = q\vec{E} + q\vec{v} \times \vec{B} = q\left(\vec{E} + \vec{v} \times \vec{B}\right) \tag{11.66}$$

where

q = electric charge on the particle
$\vec{E}$ = electric field vector
$\vec{v}$ = velocity of the particle
$\vec{B}$ = magnetic field vector

The magnetic force points in the direction of the cross product as given by the right-hand rule (Sect. 10.3.1) if q is positive, and in the opposite direction if q is negative.

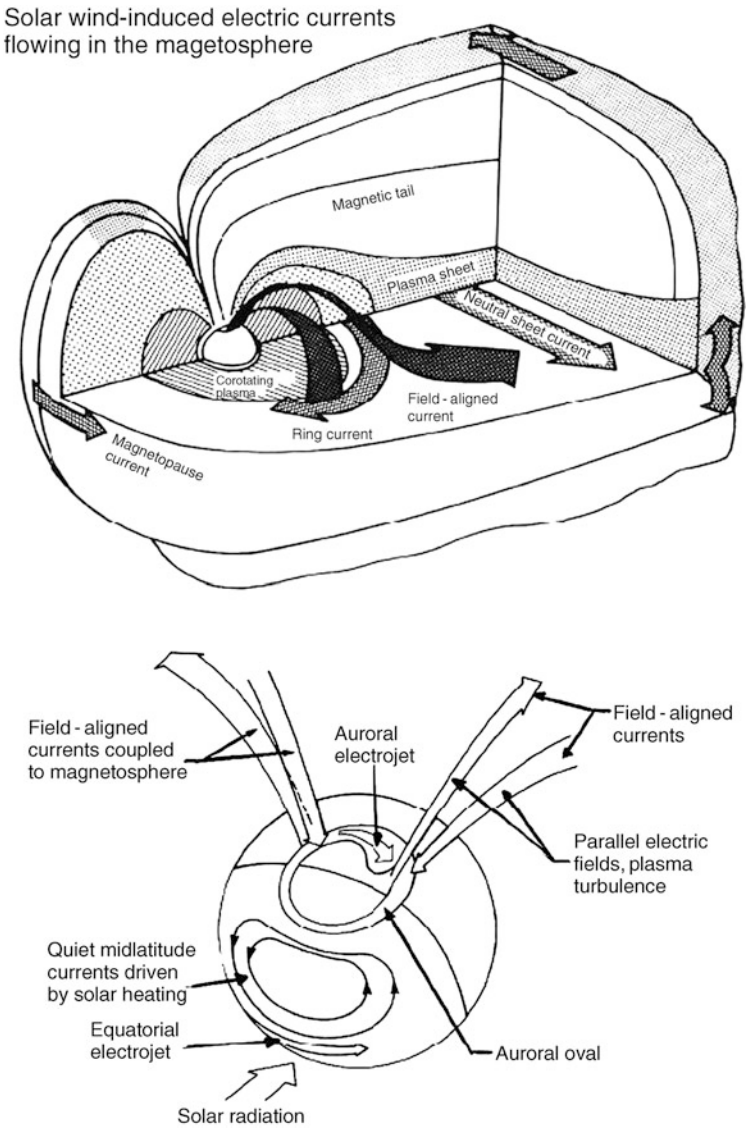

Fig. 11.9 Schematic diagrams showing where currents flow in the Earth's magnetosphere and ionosphere (from Parks 1991, Fig. 7.1, p. 244, reproduced with the author's permission.)

Equation (11.66) shows that

A. electric fields affect all charges, moving or at rest.
B. magnetic fields affect only moving charges.
C. the electric force is parallel or antiparallel to $\vec{E}$.
D. the magnetic force is perpendicular to both $\vec{v}$ and $\vec{B}$.

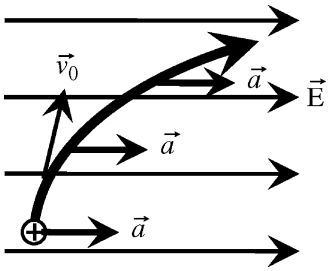

Fig. 11.10 Acceleration of a charged particle by a uniform electric field

11.5.1.2 The Gravitational Force

$$\vec{F} = m\vec{g} \tag{11.67}$$

The gravitational force on a charged particle is usually insignificant when electric and/or magnetic fields are present, but there are times when it must be included.

We now apply (11.66) to several situations relevant to the Earth's magnetosphere.

11.5.2 $\vec{E}$ Uniform and Time-Independent; $\vec{B} = 0$

With $\vec{B} = 0$, (11.1) becomes

$$\vec{F} = q\vec{E} \tag{11.68}$$

If other forces are negligible, then the acceleration of a particle of charge q and mass m is, from Newton's second law (the vector sum of all forces on an object equals the object's mass times its acceleration),

$$\vec{a} = \frac{q\vec{E}}{m} \tag{11.69}$$

Thus the electric force acting by itself accelerates particles in a direction parallel or antiparallel to the electric field, sometimes producing very large speeds.

With $\vec{E}$ constant and uniform, finding the motion of a charged particle is a straightforward constant-acceleration kinematics problem (projectile motion) as in Fig. 11.10 and is solved the same way as for a rock thrown off a cliff without air resistance. The solution in the direction parallel to $\vec{E}$ is

$$v_{||} = (v_0)_{||} + \left(\frac{qE}{m}\right)t \tag{11.70}$$

$$x_{||} = (x_0)_{||} + (v_0)_{||}t + \frac{1}{2}\left(\frac{qE}{m}\right)t^2 \tag{11.71}$$

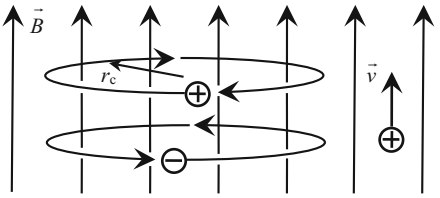

Fig. 11.11 Electric charges moving perpendicular to uniform magnetic field lines execute gyromotion; charges moving parallel to the field lines maintain constant velocity

11.5.3 $\vec{B}$ Uniform and Time-Independent; $\vec{E} = 0$

With $\vec{E} = 0$, (11.66) becomes

$$\vec{F} = q\vec{v} \times \vec{B} \tag{11.72}$$

The cross-product ensures that $\vec{F} \perp \vec{v}$ at all times; consequently, the speed, $v = |\vec{v}|$, cannot change. The perpendicular force, however, produces a continuously changing direction of travel; thus the particle's velocity changes with no change in speed.

Case 1. If $\vec{v} \perp \vec{B}$, then the magnetic force acts centripetally to produce uniform circular motion *(gyromotion* or *cyclotron motion)* in a plane perpendicular to $\vec{B}$. The radius of gyromotion, r_c, is variously called the *Larmor radius, radius of gyration, gyroradius,* or *cyclotron radius*.

Because in (11.72) the direction of $\vec{B}$ depends on the sign of q, charges of opposite sign gyrate in opposite directions. Figure 11.11 illustrates this motion for particles of equal mass and speed but opposite charge.

Centripetal acceleration is given by $a = v^2/r$, so if the magnetic force is the only force acting, and with $\vec{v} \perp \vec{B}$, Newton's second law ($\mathbf{F} = m\mathbf{a}$) becomes

$$qvB = m\frac{v^2}{r_c} \tag{11.73}$$

Solving for r_c gives

$$r_c = \frac{mv}{qB} \tag{11.74}$$

Case 2. If $\vec{v} \| \vec{B}$ (Fig. 11.11) then $\vec{F} = q\vec{v} \times \vec{B} = 0$. Thus a charged particle moving parallel to a uniform magnetic field feels no $\vec{v} \times \vec{B}$ force and continues to move in a straight line at a constant speed, parallel to $\vec{B}$, unless acted on by some other (non-magnetic) force.

Fig. 11.12 $\vec{v}$ not $||\vec{B}$

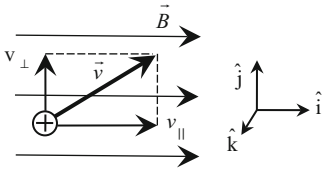

Fig. 11.13 Helical path with constant pitch angle, for a charged particle moving in a uniform magnetic field

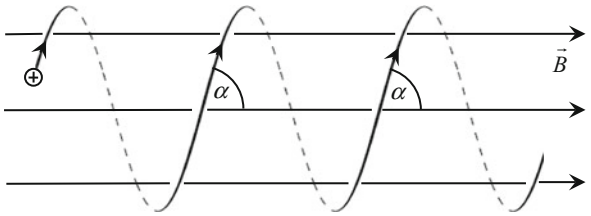

Case 3. If $\vec{v}$ is neither perpendicular nor parallel to $\vec{B}$, as in Fig. 11.13, then we can break $\vec{v}$ into components $v_\perp$ perpendicular and $v_{||}$ parallel to $\vec{B}$. Using the unit vectors $\hat{\mathbf{i}}, \hat{\mathbf{j}}, \hat{\mathbf{k}}$ defined in Fig. 11.12,

$$\vec{F} = q\vec{v} \times \vec{B} = q\left(v_{||}\hat{\mathbf{i}} + v_\perp \hat{\mathbf{j}}\right) \times B\hat{\mathbf{i}} = -qv_\perp B\hat{\mathbf{k}} \tag{11.75}$$

because $\hat{\mathbf{i}} \times \hat{\mathbf{i}} = 0$. Thus the force is due entirely to $v_\perp$, producing gyromotion with a gyroradius

$$r_c = \frac{mv_\perp}{qB} \tag{11.76}$$

Because the force has no component parallel to $\vec{B}, v_{||}$, remains constant. The particle thus moves at constant speed parallel or antiparallel to the magnetic field lines while executing circular motion perpendicular to the field lines.

The resulting path is a *helix,* as shown in Fig. 11.13. The angle, α, between $\vec{v}$ and $\vec{B}$ is called the *pitch angle* of the helix and is constant in a uniform magnetic field.

11.5.4 Guiding Center

The guiding center concept is useful in many situations involving single particles, and in multi-particle situations where the individual particles act independently. It has limitations, however; for example, it is not so useful when the particles act collectively as a fluid.

The guiding center description is based on the idea (illustrated in Fig. 11.14) that a particle "spiraling" along magnetic lines of force executes purely circular motion

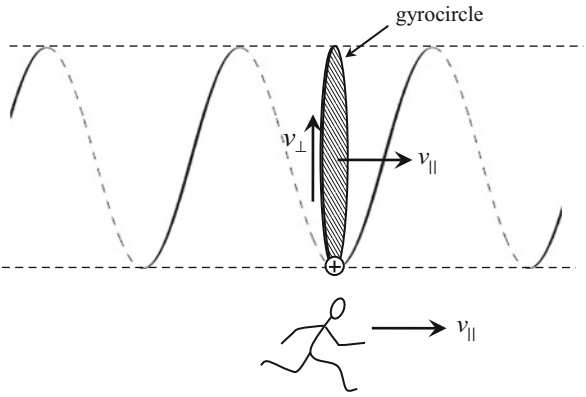

Fig. 11.14 Guiding center concept

as seen by someone moving with a vector velocity equal to $v_\parallel$. Thus the particle moves in a gyrocircle, while the center of the gyrocircle is guided in a particular direction at a particular speed by the magnetic field lines.

We now apply the gyrocircle and guiding center concepts to various situations relevant to planetary magnetospheres.

11.5.5 Diamagnetism

A charged particle executing gyromotion is equivalent to a ring of electric current of radius r_c. Conventional current is taken to be in the direction of positive charge flow or opposite to the direction of negative charge flow, as indicated in Fig. 11.15. Because positive and negative charges gyrate in opposite directions, the conventional current, I, and the resulting induced magnetic field directions are the same for both positive and negative charges, as shown in Fig. 11.15.

The application of the right-hand rule for currents,

> point the thumb of the right hand along the direction of conventional current; then the fingers curl around the current in the direction of the induced magnetic field,

or for current loops,

> curl the fingers of the right hand around the current loop in the direction of conventional current; then the thumb points in the direction of the induced magnetic field inside the loop,

in Fig. 11.15 shows that, *within* each current loop, the induced magnetic field opposes the external magnetic field, whereas *outside* (but in the same plane as) the gyromotion, the induced field is in the same direction as the external field. These characteristics identify gyromotion as *diamagnetic*.

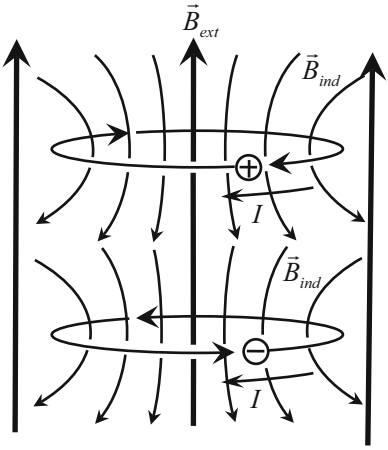

Fig. 11.15 Diamagnetic currents and induced magnetic fields

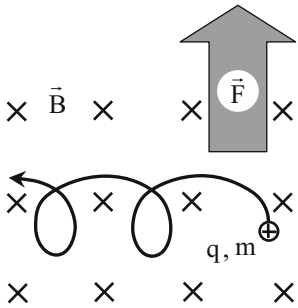

Fig. 11.16 $\vec{F} \times \vec{B}$ drift

11.5.6 $\vec{E} \times \vec{B}$ Drift and Field-Aligned Currents

In Fig. 11.16, a particle of charge q and mass m has been released at rest in a uniform, time-independent magnetic field, $\vec{B}$. In addition to the magnetic force, the particle is also subject to a constant force, $\vec{F}$, acting in a direction perpendicular to $\vec{B}$. This force might arise, for example, from a uniform electric or gravitational field in the same region of space.

As illustrated schematically in Fig. 11.16, the particle will initially accelerate in the direction of $\vec{F}$. This produces a magnetic force perpendicular to the motion, causing the particle to deviate more and more from its initial direction until it is moving perpendicular to $\vec{F}$.

Up to this point there is a component of the particle's motion in the direction of $\vec{F}$, so $\vec{F}$ does positive work on the particle, the particle's speed increases, and by (11.74) the curve has an ever-increasing radius. After this point the magnetic force deviates the particle's motion back against $\vec{F}$, the work done on the particle by $\vec{F}$ becomes negative, the particle's speed decreases, and the particle moves in a curve

of ever-decreasing radius until the motion is again perpendicular to $\vec{F}$. Both forces continue to act, and the subsequent motion is cyclic as illustrated schematically in Fig. 11.16. (Note that the curve in Fig. 11.16 is flat, and not a helix seen in perspective.)

Thus the motion is somewhat counter-intuitive: the force acting on the charged particle causes the particle to drift in a direction perpendicular to both $\vec{F}$ and $\vec{B}$. Applying the right-hand rule in Fig. 11.16 shows that a positive charge drifts in the direction of $\vec{F} \times \vec{B}$. A mathematical analysis (see the problems at the end of this chapter) gives the drift velocity, $\vec{v}_D$, as

$$\vec{v}_D = \frac{\vec{F} \times \vec{B}}{qB^2} \tag{11.77}$$

If the force is gravitational, then

$$\vec{v}_D = \frac{m\vec{g} \times \vec{B}}{qB^2} = \frac{\vec{g} \times \vec{B}}{(q/m)B^2} \tag{11.78}$$

Thus the drift speed depends on the charge-to-mass ratio of the particle; also, because of the factor q in the equation, charges of opposite sign drift in opposite directions, producing a current.

If the force arises from an electric field, $\vec{E}$, in a region of space having crossed electric and magnetic fields (Fig. 11.17), then

$$\vec{v}_D = \frac{q\vec{E} \times \vec{B}}{qB^2} = \frac{\vec{E} \times \vec{B}}{B^2} \tag{11.79}$$

The resulting motion is called $\vec{E} \times \vec{B}$ drift and is perpendicular to both $\vec{E}$ and $\vec{B}$ (in the $\vec{E} \times \vec{B}$ direction). From (11.79), $\vec{v}_D$ is independent of both q and m, so positive and negative charges drift in the same direction and (if there is charge neutrality and the charges have equal mobility) $\vec{E} \times \vec{B}$ drift does not produce a current.

The curves in Figs. 11.16 and 11.17 are examples of a *trochoid,* the curve traced by a point on the outer edge of a wheel that rolls with or without slippage; e.g., on a side-wheeler steamboat plying a lake, the rim of the paddlewheel turns faster than the boat moves forward, so a person standing on the lakeshore sees the outer edge of each paddle move forward in a long arc at the top, then dip into the water and drop back, producing the loops of the trochoid. If the wheel rolls on a solid surface without slipping, such as the wheel of a bicycle or automobile, the part of the wheel in contact with the ground is momentarily stationary and the loops in Fig. 11.17 degenerate to cusps (points). The resulting curve is a *cycloid.*

Fig. 11.17 $\vec{E} \times \vec{B}$ drift

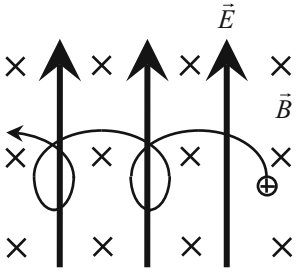

These analogies suggest that the guiding center concept remains valid for $\vec{E} \times \vec{B}$ drift: like a point on the paddlewheel, the particle moves at constant speed around a gyrocircle while the gyrocircle is guided in the $\vec{E} \times \vec{B}$ direction at the drift velocity, $\vec{v}_{\mathrm{D}}$.

If $\vec{E}$ is not perpendicular to $\vec{B}$ then take components $E_{\|}$ parallel to $\vec{B}$ and $E_{\perp}$ perpendicular to $\vec{B}$. $E_{\perp}$ causes $\vec{E} \times \vec{B}$ drift perpendicular to the magnetic field, but (for charge neutrality and charges of equal mobility) no current. $E_{\|}$ accelerates charges of opposite sign in opposite directions along the magnetic field lines, producing a current parallel to the magnetic field, i.e., a *field-aligned current*. $E_{||}$ creates a potential difference, $V = E_{||}\boldsymbol{\ell}$, over any distance $\boldsymbol{\ell}$ along a field line, so magnetic field lines in planetary magnetospheres act like conductors in electric circuits. This idea will be developed further later in this chapter.

Now return to Fig. 11.11 and consider it from a new viewpoint. In Fig. 11.11, there is no electric field, the magnetic field is at rest relative to the observer, and the positive ion in the upper left trajectory in the figure is executing simple gyromotion around the magnetic field lines. This ion has some (and always the same) velocity $\vec{v}_0$ toward the left every time it is on the near side of the gyrocircle.

Now consider this ion from the viewpoint of a different observer who is moving toward the left at constant velocity $\vec{v}_0$. This observer will see the ion momentarily at rest every time the ion is on the near side of the gyrocircle in Fig. 11.11, and will also see the gyrocenter dropping back (moving toward the right in the figure) at velocity $-\vec{v}_0$. The figure described by the ion as seen by this observer is therefore a cycloid, as described above; i.e., the ion appears to be undergoing $\vec{E} \times \vec{B}$ drift (to the right in the figure) as seen by this observer. An observer at rest relative to the magnetic field measures an electric field of zero (because the gyrocircle is closed), but an observer moving relative to the magnetic field measures a non-zero electric field (because the gyrocircle is open: a cycloid). This electric field is called a *motional electric field*, and is given by $\vec{E} = \vec{v}_0 \times \vec{B} = -\vec{v}_B \times \vec{B}$, where $\vec{v}_B$ is the velocity of the magnetic field as seen by the moving observer. (This is the same motional electric field that is generated between the wingtips of an aircraft that is flying with its wings perpendicular to the Earth's magnetic field lines.) It is left as an exercise for the reader to verify (e.g., from the right-hand rule) that the motional electric field created by the observer's motion is in the correct direction to give an $\vec{E} \times \vec{B}$ drift to the right in Fig. 11.11 as seen by the moving observer.

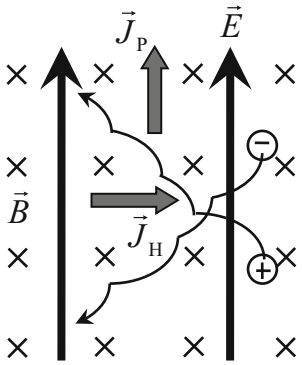

Fig. 11.18 $\vec{E} \times \vec{B}$ drift with collisions. $\vec{J}_P$ is the Pedersen current, and $\vec{J}_H$ is the Hall current

11.5.7 $\vec{E} \times \vec{B}$ Drift with Collisions

In a collisionless plasma, $\vec{E} \times \vec{B}$ drift does not produce a current if there is charge neutrality (Sect. 11.5.6). However, the lower ionosphere is sufficiently dense for collisions to be important, and each collision allows the charge to restart its motion under the influence of the electric field. As shown in Fig. 11.18, charges of opposite sign drift in opposite directions parallel or antiparallel to $\vec{E}$ while they continue to undergo $\vec{E} \times \vec{B}$ drift in the same direction perpendicular to $\vec{E}$. The former of these two drifts gives rise to a current, referred to in the ionosphere as the *Pedersen current,* parallel to $\vec{E}$.

In a collision-dominated plasma, $\vec{E} \times \vec{B}$ drift also creates a current, despite charge neutrality, because the smaller gyroradii and higher speeds of the electrons give them greater mobility than the ions. The resulting *Hall current* is perpendicular to both $\vec{E}$ and $\vec{B}$, but opposite to the $\vec{E} \times \vec{B}$ direction (Fig. 11.18). The Pedersen and Hall currents will be important when discussing ionospheric currents and aurorae (Sect. 11.6.7).

The energy given to the ions and electrons of the plasma by the electric field is dissipated as heat through collisions of the plasma particles with (primarily) neutral ionospheric atoms, since neutrals far outnumber ions in the ionosphere. This process, in which the work done on the plasma particles by the electric field is dissipated as heat, is referred to as *ohmic losses* or *joule heating*. If in Fig. 11.18 a particle of species i (i.e., an ion or an electron) and charge q_i moves through a displacement $d\vec{\boldsymbol{\ell}}$ along the path in time dt, then the infinitesimal quantity of work done on this particle by the electric field in time dt is

$$\delta W = d\vec{\boldsymbol{\ell}} \bullet \vec{F} = q_i d\vec{\boldsymbol{\ell}} \bullet \vec{E} \tag{11.80}$$

The rate of joule heating (= power dissipated, P_i) by any species i per unit volume is then

$$P_i = n_i \delta W/dt = n_i q_i d\vec{\ell} \bullet \vec{E}/dt = n_i q_i \vec{v}_i \bullet \vec{E} = \vec{J}_i \bullet \vec{E} \tag{11.81}$$

where n_i, $\vec{v}_i$ and $\vec{J}_i = n_i q_i \vec{v}_i$ are the number density, velocity and current density of species i, respectively. (Note that in Fig. 11.18 we have assumed that the neutral medium is at rest; therefore, $\vec{E}$ is the electric field measured in the rest frame of the neutral medium.) The total current density and power dissipated are $\vec{J} = \sum \vec{J}_i$ and

$$P = \sum P_i = \vec{J} \bullet \vec{E} \tag{11.82}$$

The treatment above assumes that the neutral gas remains at rest in the chosen reference frame and the plasma particles move through it. In fact, momentum transfer requires that some energy from the electric field is converted to bulk motion of the neutral gas; thus, the result above gives an upper limit to the amount of joule heating. Nevertheless, the dot product shows that only the component of $\vec{J}$ parallel to $\vec{E}$ contributes to joule heating; i.e., the Pedersen current is dissipative, because $\vec{J} \bullet \vec{E} > 0$ and the Hall current is dissipationless, because $\vec{J} \bullet \vec{E} = 0$.

Joule heating can be considerable in the ionosphere. Within an active aurora, it can amount to tens or even hundreds of kilowatts per square kilometer of sky within active aurorae (Knudsen, D. J. 2013, *private communication*). Figure 11.19 shows an active aurora on the Earth, photographed from the International Space Station.

For an alternative treatment of this topic in the reference frame of the plasma, where the dissipation turns out to be by friction between the plasma and the gas rather than by joule heating (i.e., the relationship is not simply $\vec{J} \bullet \vec{E}$), see Vasyliūnas and Song (2005).

11.5.8 Polarization Drift

We now examine the situation where $\vec{B}$ is uniform in space and constant in time and $\vec{E}$ is uniform in space and constant in direction, but changes in magnitude with time, i.e., $dB/dt = 0$ but $dE/dt \neq 0$. Figure 11.20 illustrates the case where E increases with time.

Both particles in Fig. 11.20 undergo $\vec{E} \times \vec{B}$ drift toward the left, but because $\vec{E}$ is increasing in strength, each particle's kinetic energy at the midpoint of any cycle is insufficient to allow it to return to its initial level in the diagram at the end of the cycle. Positive charges therefore drift parallel to $\vec{E}$ and negative charges drift antiparallel to $\vec{E}$ while both undergo $\vec{E} \times \vec{B}$ drift perpendicular to $\vec{E}$ and $\vec{B}$. The drift parallel or antiparallel to $\vec{E}$ is called *polarization drift*.

Fig. 11.19 Aurora over the southern Indian Ocean, photographed from the International Space Station on September 17, 2011. Although aurorae are usually seen only at high northern and southern latitudes, this one occurred during a geomagnetic storm, resulting from a coronal mass ejection that left the Sun on September 14, 2011. Credit: NASA/Goddard Space Flight Center

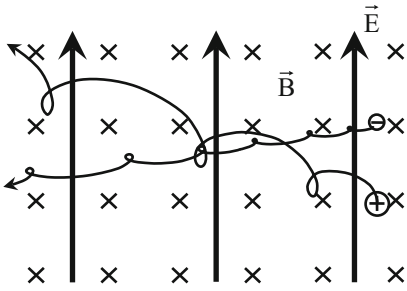

Fig. 11.20 Polarization drift $||\vec{E}$ with $\vec{E} \times \vec{B}$ drift $\perp \vec{E}$

In this case, the drift velocity of the guiding center consists of two components:

1. $\vec{v}_D$, the $\vec{E} \times \vec{B}$ drift velocity perpendicular to $\vec{E}$ and $\vec{B}$, described in Sect. 11.5.6; but note that v_D is increasing with time because E is increasing with time, so from (11.79) the cycles in Fig. 11.20 become increasingly stretched.
2. $\vec{v}_P$, the polarization drift velocity parallel or antiparallel to $\vec{E}$, given by

$$\vec{v}_P = -\frac{m}{qB^2}\left(\frac{d\vec{v}_D}{dt}\right) \times \vec{B} \tag{11.83}$$

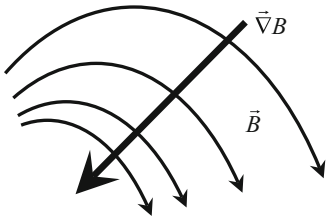

Fig. 11.21 Curvature and gradient in an inhomogeneous magnetic field

It follows from (11.79) and (11.83) that

$$\vec{v}_{\mathrm{P}} = -\frac{m}{qB^2}\frac{\mathrm{d}\vec{E}}{\mathrm{d}t} \tag{11.84}$$

Polarization drifts are in opposite directions for opposite charges, so polarization drift produces a current parallel to $\vec{E}$.

11.5.9 Gradient and Curvature Drift

We now investigate inhomogeneous, time-independent magnetic fields, in the absence of electric fields.

It is unusual for a magnetic field to be uniform. Figure 11.21 provides a schematic illustration of a more typical magnetic field (e.g., a magnetic dipole field): the field lines are curved, and the magnetic field strength, B, increases toward the center of curvature.

Thus, real magnetic fields generally show both curvature and gradient.

11.5.9.1 Gradient Drift

Figure 11.22 illustrates schematically a region of space containing a magnetic field gradient. Here, we temporarily neglect curvature. From (11.74), the gyroradius is smaller where B is greater and *vice versa,* so a positive particle follows a trochoid, as shown. A negative particle initially traveling downward will curve to the left in Fig. 11.22, so positive and negative charges drift in opposite directions and gradient drift produces a current.

If the magnetic field gradient is small ($\Delta \mathrm{B} << B$ over a gyroradius) then $\vec{B}$ is approximately uniform over the gyrocircle and the guiding center concept is still valid: the particle moves in a gyrocircle which does not quite close on itself, resulting in a drift of the guiding center perpendicular to both $\vec{B}$ and $\vec{\nabla}B$. Taking the y-axis in the direction of the gradient (upward in Fig. 11.22), the drift speed is

$$v_{\nabla B} = \frac{mv_{\perp}^2}{2qB^2}\frac{\partial B}{\partial y} \tag{11.85}$$

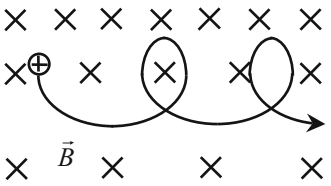

Fig. 11.22 Gradient drift

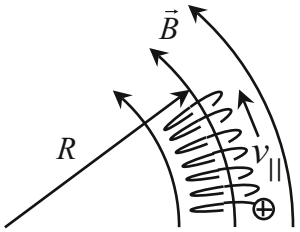

Fig. 11.23 Curvature drift

11.5.9.2 Curvature Drift

Figure 11.23 illustrates a hypothetical magnetic field which has curvature, but no gradient. Charged particles follow helical paths along the field lines, as indicated. Because we are neglecting the field gradient, there is no gradient drift in Fig. 11.23. However, the particles can follow a curved field line only if there is a centripetal force

$$F_{\text{cent}} = \frac{mv_{||}^2}{R} \tag{11.86}$$

acting on them, directed toward the center of curvature. This force must arise from the motion of the particle and, in fact, is created by a drift of the particle across the field lines with a drift speed v_C (where "C" signifies *curvature drift*). Then from (11.72),

$$\vec{F}_{\text{cent}} = q\vec{v}_C \times \vec{B} \tag{11.87}$$

From the right-hand rule, with q positive in Fig. 11.23, $\vec{F}_{\text{cent}} = \vec{v}_C$ must be out of the page to give a force toward the center of curvature. From (11.87), negative charges drift into the page, so curvature drift in Fig. 11.23 produces a current out of the page. This result is independent of which direction the particle follows along the field line (upward or downward in Fig. 11.23), because the direction of the centripetal force must be toward the center of curvature in both cases.

The curvature drift speed is given by

$$v_C = \frac{m v_\parallel^2}{qB^2} \frac{\partial B}{\partial y} \tag{11.88}$$

In fact, in a curved magnetic field the field strength increases toward the center of curvature, so gradient and curvature drift act together. Compare Fig. 11.23 to Fig. 11.22 (rotated by some appropriate angle) to see that the gradient drift in Fig. 11.23 is then also out of the page, and the gradient and curvature drift speeds add. The resulting total drift speed, referred to here as $v_{C\nabla B}$, is

$$v_{C\nabla B} = v_C + v_{\nabla B} = \frac{m}{qB^2}\left(v_\parallel^2 + \frac{1}{2}v_\perp^2\right)\frac{\partial B}{\partial y} \tag{11.89}$$

We now discuss various current systems that arise from the interactions described in Sect. 11.5.

11.6 Electric Currents in the Ionosphere and Magnetosphere

11.6.1 The Ionospheric Dynamo

11.6.1.1 The S_q ("Solar Quiet") Current System

The S_q current system is caused primarily by solar heating, and to a smaller extent by solar tides. The atmosphere over a given region of the Earth expands as it is heated in the morning and contracts as it cools later in the afternoon. This motion drives ionospheric electrons and ions across magnetic field lines, generating currents in the ionosphere (Fig. 11.9). The resulting current pattern remains at rest as seen from the Sun, as the Earth rotates under it.

The term "solar quiet" refers to the absence of solar activity (e.g., at solar minimum) such as solar flares, which can modify the current pattern.

Any current system creates magnetic fields, and these modify the observed magnetic field at a given location on the Earth. Thus, as an observer's location rotates under the ionospheric current system, the observer sees a daily variation in the magnetic field.

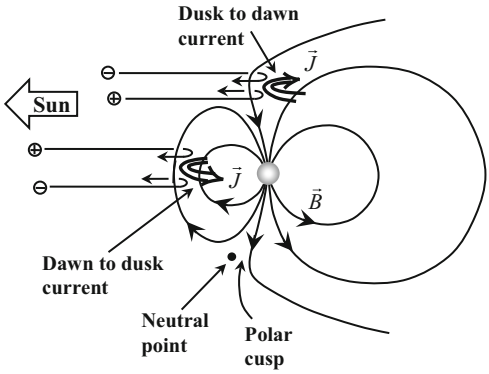

Fig. 11.24 Schematic illustration of the interaction of solar wind particles with the Earth's magnetosphere, and the formation of the Chapman-Ferraro boundary current. In reality, the radius of gyration of positive ions is much greater than that of electrons. The view is from the dusk side of the Earth

11.6.1.2 The L_q ("Lunar Quiet") Current System

The L_q current system is caused primarily by lunar tides and remains at rest as seen from the Moon as the Earth rotates under it.

Of the atmospheric tides, the solar thermal tide is stronger than either the lunar or solar gravitational tides, and the lunar gravitational tide is stronger than the solar gravitational tide.[6] The ionospheric dynamo is thus dominated by solar heating, with the next strongest influence being the lunar tide.

11.6.2 Boundary Current

The *boundary current,* a.k.a. *magnetopause current* or *Chapman-Ferraro current,* is a diamagnetic current (Sect. 11.5.5) formed by the interaction of the solar wind with the Earth's magnetosphere at the magnetopause. Figure 11.24 illustrates schematically the principles involved.

The right-hand rule (Sect. 11.5.5) shows that positive ions in the solar wind gyrate out of the page when they encounter the Earth's magnetic field, and electrons gyrate into the page. The resulting current direction is out of the page, or from dawn to dusk (see Fig. 11.32 for orientations). Individual particles in this current are simply performing an arc of gyration, rather than flowing in the manner of a conduction current.

From the right-hand rule, the induced magnetic field of the boundary current opposes the Earth's magnetic field on the sunward side and strengthens it on the side facing the Earth, in effect compressing the magnetic field on the noon side of the Earth. Above and below, field lines that would have closed on the sunward side are swept

[6] This is because the differential gravitational force is proportional to r^{-3}.

back to the magnetotail by the same process, with the solar wind particles creating a dusk to dawn diamagnetic current that provides closure for the dawn-to-dusk current.

A *neutral point,* or a point of zero magnetic field, marks where the field lines diverge above each polar cap. As Fig. 11.24 shows, the neutral points are sunward of the Earth. A *polar cusp,* a region of funnel-shaped magnetic field lines, surrounds each neutral point. The polar cusps can guide solar wind particles into the atmosphere. As these particles travel along the magnetic field lines, they are accelerated by field-aligned electric fields, and are energetic enough by the time they reach the atmosphere to generate dayside aurorae.

The acceleration is an important part of this process: Solar wind particles have energies of only tens of eV, whereas spacecraft passing through the cusp measure electron energies of hundreds of eV associated with diffuse red auroral glow and several keV associated with dayside auroral arcs (Knudsen, D. J. 2013, *private communication*). Thus, the magnetosphere has to provide field-aligned electric fields to accelerate them. How these electric fields arise is an area of active research.

An increase in the solar wind flux results in an increase in the boundary current. This in turn causes an increase in the magnetic field strength at the Earth's surface and marks the onset of a magnetic storm (Sect. 11.6.4).

11.6.3 Ring Current

11.6.3.1 Magnetic Mirrors

Figure 11.25 shows a positively charged particle following a helical path into a region of converging magnetic field lines. Using the guiding center concept, we may describe the particle at any given instant as moving at speed $v_\perp$ in a gyrocircle of radius r_c, while the center of the gyrocircle follows the central field line to the right at speed $v_{||}$. We now look at the subsequent motion of this particle.

If the field lines converge at angle θ relative to the central field line, then the Lorentz force, $\vec{F}_B = q\vec{v} \times \vec{B}$, on the particle is also at angle θ to the plane of the gyrocircle, as indicated in Fig. 11.25. The components of F_B perpendicular and parallel to the central field line are then

$$F_\perp = F_B \cos\theta \tag{11.90}$$

$$F_{||} = F_B \sin\theta \tag{11.91}$$

$F_\perp$ produces gyromotion, while $F_{||}$ acts to change $v_{||}$. The speed of the guiding center thus increases or decreases, depending on the relative directions of $F_{||}$ and $v_{||}$. (In Fig. 11.25, $v_{||}$ would decrease.)

$F_{||}$ depends only on q, B, $v_\perp$ (through F_B), and θ and is independent of $v_{||}$. Thus, in Fig. 11.25, if the guiding center is brought to rest, it will immediately start to move with increasing speed toward the left, i.e., the converging field lines form a magnetic mirror, reflecting incoming particles back toward the region of weaker field.

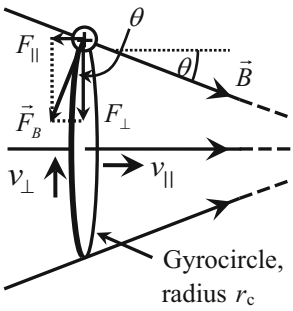

Fig. 11.25 A charged particle in a region of converging magnetic field lines

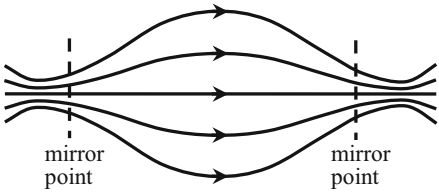

Fig. 11.26 Magnetic bottle

Two magnetic mirrors opposing each other form a magnetic bottle (Fig. 11.26), providing one of the methods proposed for containing the million-degree plasma in a fusion reactor.

11.6.3.2 Characteristics of the Motion

We now look for constants of the motion for the particle in Fig. 11.25. We take the case where:

A. The magnetic field is constant in time as seen by an external observer (the particle, however, encounters a changing magnetic field as it moves through the converging field lines).

B. The field lines are not necessarily straight, but they converge symmetrically about the central field line of the particle's motion, and the magnetic field strength is uniform over any given plane perpendicular to the central field line, although it changes from one plane to the next along the field line.

C. The rate of convergence of the magnetic field lines is "slow;" i.e., the angle θ in Fig. 11.25 is small, so that $\cos\theta \approx 1$. Then, over any one gyrocircle, the change in the gyroradius is small compared to the gyroradius itself.

The particle then moves in a gyrocircle, the radius of which changes as the magnetic field strength changes, and the speed and direction of travel of which change because of $F_{\|}$.

Gyromotion can be regarded as a current loop in which the current consists of one particle of charge q passing a given point on the gyrocircle f times per second. f is referred to as the *frequency of gyration*. The magnetic moment of a current loop is

$$\mu_B = IA \tag{11.92}$$

where I is the current and A is the area of the loop. The magnetic moment of the gyromotion can then be shown to be (see the problems in the Challenges section at the end of this chapter)

$$\mu_B = \frac{qr_c v_\perp}{2} \tag{11.93}$$

The angular momentum of a particle of mass m moving with speed $v_\perp$ in a gyrocircle of gyroradius r_c is

$$L = mv_\perp r_c \tag{11.94}$$

From (11.93) and (11.94) we obtain

$$\mu_B = \frac{qL}{2m} \tag{11.95}$$

The torque on a particle equals the rate of change of its angular momentum:

$$\tau = \frac{\mathrm{d}L}{\mathrm{d}t} \tag{11.96}$$

However, the torque exerted on a charged particle by the magnetic force is zero; hence, from (11.96), the angular momentum of a particle undergoing gyromotion does not change with time and is a constant of the motion. It then follows from (11.95) that the magnetic moment, μ_B, is also a constant of the motion.

Because we are taking the case where B is uniform over the gyrocircle, the magnetic flux through the gyrocircle is

$$\Phi_B = BA \tag{11.97}$$

It then follows from previous results that

$$\Phi_B = \frac{2\pi m}{q^2}\mu_B \tag{11.98}$$

Hence, Φ_B is also a constant of the motion.

It can also be shown that the particle's kinetic energy, $K = 1/2mv^2$, is a constant of the motion, and hence, from Pythagoras' theorem,

$$\frac{1}{2}mv^2 = \frac{1}{2}mv_\perp^2 + \frac{1}{2}mv_\parallel^2 = \text{const} \tag{11.99}$$

The results above show that, for a particle undergoing gyromotion, Φ_B, L, and K are constants of the motion. As the magnetic field changes, r_c changes to conserve the magnetic flux through the gyrocircle. As r_c changes, $v_\perp$ changes to conserve angular momentum; and as $v_\perp$ changes, $v_\parallel$ changes to conserve kinetic energy.

For the case where the particle is moving toward increasing B, as in Fig. 11.25, (11.99) shows that if $v_\perp$ becomes equal to v then $v_\parallel = 0$ and further progress is impossible. $F_\parallel$, however, is non-zero and pushes the particle back toward weaker magnetic field. For a symmetrical magnetic bottle, as in Fig. 11.26, the particle will mirror back and forth inside the bottle without contacting any physical walls, making magnetic bottles very useful for fusion reactors operating at millions of degrees temperature.

11.6.3.3 Trapping and Precipitation

The inner magnetic field lines in Fig. 11.24 (i.e., those not extending off down the magnetic tail) form a curved analog of Fig. 11.26 and cause charged particles to mirror back and forth between the northern and southern hemispheres. In the Earth's magnetosphere, these regions of trapped charged particles are the *Van Allen radiation belts,* consisting of an inner belt of high-energy protons (10–100 MeV) at distances of ~1–3R_E above the Earth's surface and an outer belt of high-energy electrons (0.1–10 MeV) and ions at ~1–10R_E above the Earth's surface, peaking in electron density between 2.3 and 3R_E above the surface. The protons in the inner belt are produced by β-decay of neutrons created by cosmic ray collisions with nuclei in the upper atmosphere.

If one of these particles enters the atmosphere before mirroring then collisions in the atmosphere will prevent it from reflecting. This loss of particles from the trapping region is known as *precipitation*.

The three constants of the motion found in Sect. 11.6.3.2 allow the magnetic field strength, B_R, to be found at the mirror point (the subscript, R, signifies "reflection") for any given pitch angle, α_0, and magnetic field strength, B_0, at the magnetic equator (the location where the magnetic field is weakest). Some relevant parameters are illustrated in Fig. 11.27. At the magnetic equator, for a particle of speed v, we can define

$$v_\parallel^0 = v\cos\alpha_0 \tag{11.100}$$

$$v_\perp^0 = v\sin\alpha_0 \tag{11.101}$$

At the mirror point,

$$v_\parallel^R = 0 \tag{11.102}$$

and therefore, from the constancy of the kinetic energy in (11.99),

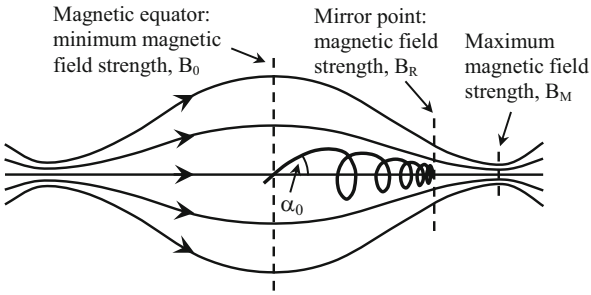

Fig. 11.27 Parameters for a magnetic mirror. α_0 is the pitch angle at the magnetic equator

$$v_{\perp}^{\mathrm{R}} = v \tag{11.103}$$

From (11.94), (11.103), and the constancy of the angular momentum, we obtain

$$v_{\perp}^{0} r_{\mathrm{c}}^{0} = v_{\perp}^{R} r_{\mathrm{c}}^{R} = v r_{\mathrm{c}}^{R} \tag{11.104}$$

Then

$$\frac{r_{\mathrm{c}}^{0}}{r_{\mathrm{c}}^{R}} = \frac{v}{v_{\perp}^{0}} \tag{11.105}$$

Finally, from the remaining characteristic of the motion, the constancy of the magnetic flux within the gyrocircle, we have

$$B_0 \pi \left(r_{\mathrm{c}}^{0}\right)^2 = B_R \pi \left(r_{\mathrm{c}}^{R}\right)^2 \tag{11.106}$$

from which, with (11.101) and (11.105),

$$B_R = B_0 \left(\frac{r_{\mathrm{c}}^{0}}{r_{\mathrm{c}}^{R}}\right)^2 = B_0 \left(\frac{v}{v_{\perp}^{0}}\right)^2 = B_0 \left(\frac{v}{v \sin \alpha_0}\right)^2 \tag{11.107}$$

or

$$B_R = \frac{B_0}{\sin^2 \alpha_0} \tag{11.108}$$

Thus, the magnetic field strength at the mirror point depends only on B_0 and α_0 and is independent of the charge, mass, and kinetic energy of the particle. Equation (11.108) shows that, in a magnetic bottle such as that in Fig. 11.27, particles of smaller α_0 mirror at larger B_0, i.e., closer to the point of maximum field strength, $B_{\max}$. If the field strength, B_{R}, required at the mirror point [from (11.108)] is greater than $B_{\max}$ then the bottle is unable to constrain these particles, and they escape through the ends of the bottle. The *critical pitch angle* at the

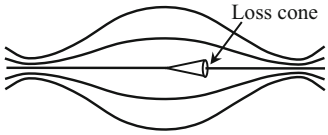

Fig. 11.28 The loss cone. All particles traveling within the loss cone (angular radius α_C) at the magnetic equator escape from the magnetic bottle

magnetic equator, α_C, so called because all particles of $\alpha_0 < \alpha_C$ escape, is obtained by setting $B_R = B_{max}$ in (11.108), yielding

$$\alpha_C = \sin^{-1}\sqrt{\frac{B_0}{B_{max}}} = \sin^{-1}\frac{1}{\sqrt{\mathfrak{R}}} \tag{11.109}$$

where the *mirror ratio*

$$\mathfrak{R} \equiv \frac{B_{max}}{B_0} \tag{11.110}$$

is the ratio of the strongest to the weakest magnetic field strength. α_C defines the *loss cone*, as illustrated in Fig. 11.28. A similar loss cone exists for particles traveling toward the left.

In similar fashion, the loss cone in a planetary magnetosphere separates particles that are lost by precipitation into the atmosphere from those that mirror. B_M is then the magnetic field strength at the exobase, where collisions are frequent enough to remove the particles.

If a process injects particles into a planetary magnetosphere with an initially isotropic distribution of pitch angles at the magnetic equator, then the fraction, f, of these particles that are precipitated equals the fraction of half a sphere [2π steradians (sr)] taken up by the loss cone. (There are 4π sr in a complete sphere, but only half of the particles are traveling toward any given end of the magnetic bottle in Fig. 11.28.) To find the fraction precipitated we first need to find the solid angle, Ω, taken up by a cone of angular radius α_c, then take the ratio of this result to 2π sr.

In Fig. 11.29, the area on the surface of the sphere intersected by the loss cone is

$$\begin{aligned} A &= \int_{\alpha=0}^{\alpha_C} dA = \int_{\alpha=0}^{\alpha_C} 2\pi r \; ds = \int_{\alpha=0}^{\alpha_C} 2\pi (a\sin\alpha)(a d\alpha) \\ &= 2\pi a^2 \int_{\alpha=0}^{\alpha_C} \sin\alpha d\alpha = 2\pi a^2 \left(1 - \cos\alpha|_{\alpha=0}^{\alpha_C}\right) \end{aligned}$$

or

$$A = 2\pi a^2 (1 - \cos\alpha_C) \tag{11.111}$$

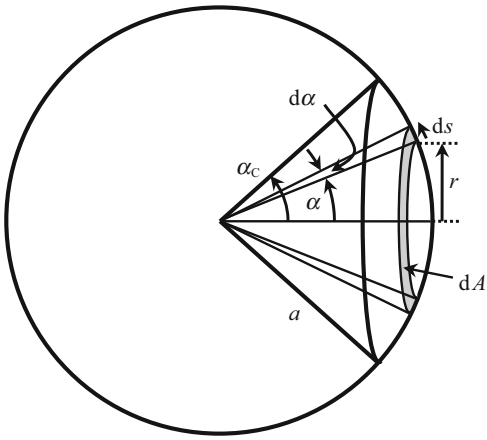

Fig. 11.29 Quantities required to find the solid angle in steradians taken up by a loss cone of angular radius α_C

The fraction of particles that are precipitated is then

$$f = \frac{\Omega}{2\pi} = \frac{1}{2\pi}\left(\frac{A}{a^2}\right) = \frac{1}{2\pi}\frac{2\pi a^2(1-\cos\alpha_C)}{a^2} = 1-\cos\alpha_C$$
$$= 1-\sqrt{1-\sin^2\alpha_C} = 1-\sqrt{1-\frac{B_0}{B_M}}$$

from (11.96) or

$$f = 1-\sqrt{1-\frac{1}{\mathfrak{R}}} \tag{11.112}$$

11.6.3.4 The Ring Current

Figure 11.30a illustrates schematically the path of a charged particle trapped in a planetary magnetosphere, mirroring back and forth between the northern and southern magnetic poles. Gradient and curvature drift (Sect. 11.5.9) cause positive charges to drift out of the page and negative charges to drift into the page in this region of the diagram, creating a current, the *ring current,* in the direction shown.

In the Earth's magnetosphere, the ring current is carried by the outer Van Allen radiation belt and is strongest in the region ~2–4R_E above the Earth's surface. As illustrated in Fig. 11.30b, the induced magnetic field within the ring current opposes the intrinsic magnetic field in the region between the ring current and the Earth's surface and reduces the measured magnetic field at any point on the Earth's surface.

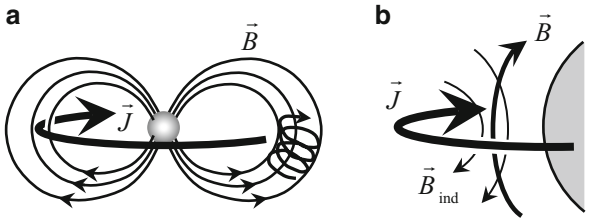

Fig. 11.30 The ring current. (**a**) The *helix* shows part of the path of a charged particle mirroring between the northern and southern hemispheres. The *heavy arrow* shows the direction of the gradient and curvature drift of a positively charged particle, and the resulting current direction. (**b**) Within the ring's radius, the induced magnetic field of the ring current opposes the intrinsic magnetic field of the Earth

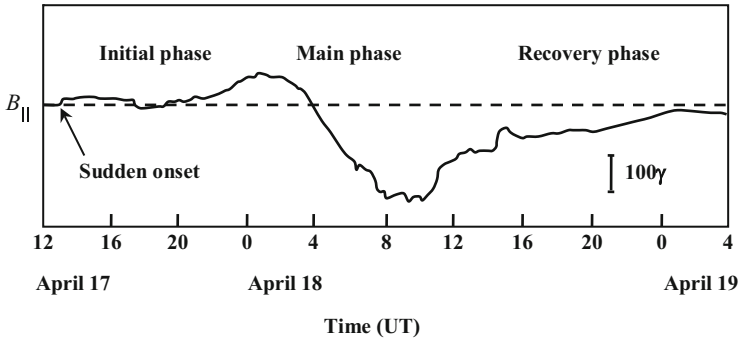

Fig. 11.31 Magnetic storm recorded at Guam. The horizontal component of the Earth's magnetic field is shown as a function of universal time (UT). The tracing has been redrawn and slightly smoothed. After Cahill 1968, Fig. 1, p. 264

11.6.4 Magnetic Storms

A *magnetic storm* (Fig. 11.31) is a worldwide disturbance in the horizontal component, $B_{||}$, of the geomagnetic field at the Earth's surface. The initial phase typically begins with a sudden onset in which B increases by several to several tens of gammas ($1\gamma = 1$ nT) in a few minutes, and lasts from tens of minutes to several hours. The main phase, where $B_{||}$ decreases below its pre-storm value, typically lasts from several hours to about 2 days, and recovery can take from several days to a month, depending on the strength of the storm. For comparison, the Earth's magnetic field strength at the surface is about 30,000–60,000 nT.

The sudden onset and initial phase occur when an enhancement in the solar wind flux, e.g., from a solar flare, encounters the Earth's magnetosphere, increasing the boundary current and compressing the magnetosphere on the Earth's dayside (Sect. 11.6.2). After some delay, the main phase of the storm begins as processes in the magnetosphere inject charged particles into the outer van Allen belt,

increasing the ring current (Sect. 11.6.3). Precipitation through the loss cone produces diffuse (mostly subvisual) aurorae, whereas the bright auroral arcs are produced by particles from further out in the plasma sheet, at ~6 Earth radii, being accelerated along magnetic field lines into the auroral oval by field aligned electric fields (Knudsen, D. J. 2013, *private communication*). The recovery phase occurs as the ring current slowly dies back and the magnetosphere returns to its undisturbed state.

Magnetic storms fall into two broad categories, related to the particle source regions on the Sun. Strong magnetic storms occur individually and result from transient high-energy phenomena: solar flares and coronal mass ejections (CME). Weaker magnetic storms often recur with a 27-day period, equal to the synodic rotation period of the Sun, and result from relatively steady streams of particles from coronal holes in the Sun's polar regions sweeping past the Earth as the Sun rotates.

The decay of the ring current during the recovery phase requires particle loss outside the loss cone, which occurs at least in part by charge-exchange interactions of ring-current ions with exospheric neutral hydrogen (Sect. 10.4.1.4). The large pressure scale height of hydrogen results in a density of $\sim 10^9$ H atoms/m^3 at the inner edge of the ring current and $\sim 10^8$ m^{-3} at geosynchronous orbit ($6.6R_E$). Fast ions capture an electron from a slow-moving H atom, resulting in a fast-moving neutral atom and a slow-moving proton. The spherical volume of neutral H surrounding the Earth is detectable by reflected UV light as the *geocorona*.

The decay processes operate continuously, so the existence of a steady ring current outside magnetic storms shows that, even in quiet times, the outer radiation belt is continuously replenished on timescales of a few days.

11.6.5 Magnetospheric Convection

The solar wind outside the magnetopause exerts a viscous drag on the plasma inside the magnetosphere, arising through waves and particle diffusion across the magnetopause. [Viscous drag occurs when two media (here, the solar wind and magnetospheric plasma) that are moving relative to each other interact as fluids.] This interaction creates a boundary layer just inside the magnetopause in which magnetospheric plasma flows antisunward at some fraction of the solar wind speed. Continuity then requires a return flow through the rest of the magnetosphere. These particles pass the Earth and rejoin the boundary particles to complete the circulation.

Currents created by the interaction of this flow with the Earth's magnetic field in turn modify the magnetic field in such a way that the magnetic field lines can be regarded as being carried with the particles as they move, stretching the magnetosphere into a long magnetotail in the antisunward direction. This continuous circulation of particles and magnetic field down and back up the magnetotail is known as *magnetospheric convection*.

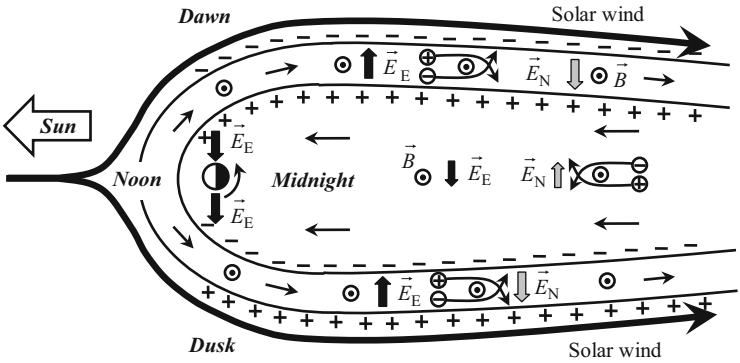

Fig. 11.32 Magnetospheric convection (Not to scale)

Figure 11.32 illustrates magnetospheric convection, looking down on the equatorial plane from above the North Pole of the Earth. The Earth rotates in the direction indicated. Directions in the magnetosphere are denoted by whether they are above the dawn, noon, dusk, or midnight point on the Earth's equator. Illustrative positive and negative charges are shown in each region, and circled dots denote magnetic field out of the page (south to north).

In the boundary layer, convection of charges past magnetic field lines creates a magnetic force in the dawn-to-dusk direction on positive charges and dusk-to-dawn on negative charges. These directions are reversed in the return flow. Magnetic forces can be modeled as arising from *non-electrostatic electric fields*, $\vec{E}_{\mathrm{N}}$ (grey arrows), by treating the magnetic force as if it were a non-electrostatic electric force arising from a non-electrostatic electric field, $\vec{F}_{\mathrm{B}} = \vec{F}_{\mathrm{N}} = q\vec{E}_{\mathrm{N}}$. Then

$$\begin{aligned} q\left(\vec{v} \times \vec{B}\right) &= q\vec{E}_{\mathrm{N}} \\ \therefore\ \vec{E}_{\mathrm{N}} &= \vec{v} \times \vec{B} \end{aligned} \tag{11.113}$$

Thus, $\vec{E}_{\mathrm{N}}$ is in the $\vec{v} \times \vec{B}$ direction, from dawn to dusk in the boundary layer, and dusk to dawn in the return flow (Fig. 11.32).

$\vec{E}_{\mathrm{N}}$ produces charge distributions at the interfaces between the boundary layer and the solar wind, and between the boundary layer and the return flow, as shown in Fig. 11.32. These charge distributions in turn produce *electrostatic fields*, $\vec{E}_{\mathrm{E}}$ (black arrows), in the dusk-to-dawn direction in the boundary layer and dawn-to-dusk in the return flow, as indicated.

Magnetospheric convection also creates electric fields, and therefore electric currents, in the ionosphere near each pole. This produces the *auroral oval,* the *eastward and westward electrojets* (part of the auroral oval), and other phenomena.

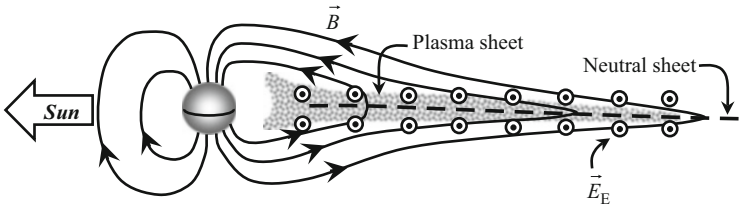

Fig. 11.33 The magnetotail neutral sheet and plasma sheet

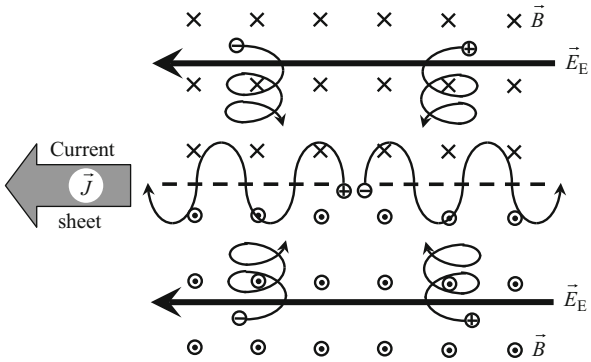

Fig. 11.34 $\vec{E} \times \vec{B}$ drift and the magnetotail current sheet

11.6.6 The Magnetotail Current Sheet

Figure 11.33 illustrates schematically (not to scale) a vertical cross-section through the magnetosphere. The dashed line denotes the neutral sheet and the circled dots denote the electrostatic field in the magnetotail, directed from dawn to dusk (toward the viewer).

Figure 11.34 shows a view in the magnetotail, facing toward the Earth (i.e., looking toward the left from the right edge of Fig. 11.33). The dashed line again denotes the neutral sheet, with magnetic field away from the observer on the north side (above) and toward the observer on the south side (below).

In regions away from the neutral sheet, positive and negative charges undergo $\vec{E} \times \vec{B}$ drift toward the neutral sheet. Because they drift in the same direction, this motion does not give rise to a current. The resulting collection of electrons and ions near the neutral sheet is the *plasma sheet* (see Fig. 11.33) Positive and negative charges in the plasma sheet now drift in opposite directions as they oscillate across the neutral sheet, producing a dawn-to-dusk current density, variously called the *neutral sheet current, magnetotail current sheet,* or *cross-tail current*.

The return flow on the outside of the magnetotail in Fig. 11.9 is in the same direction as the return flow of the dayside boundary current (Sect. 11.6.2). These two flows merge near the Earth.

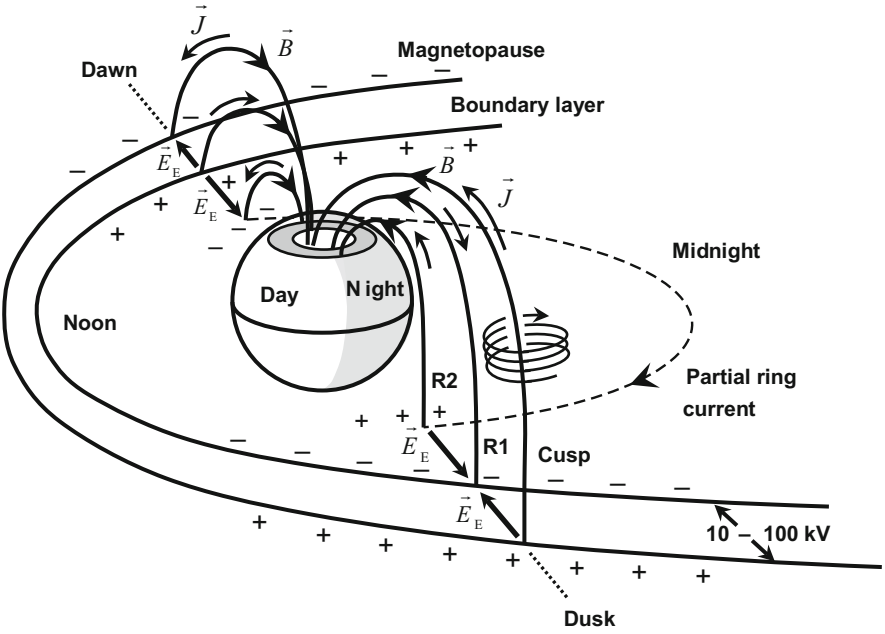

Fig. 11.35 Coupling of the low-latitude magnetosphere and boundary layer to the northern ionosphere (not to scale). The magnetic field lines act as electrical conduits connecting the convection emf in the boundary layer to the polar cap (*white ellipse*) and the convection emf in the magnetosphere to the auroral oval (*grey ring*). The cusp field-aligned current (FAC) connects the magnetopause to the polar cusp in the noon region of the polar cap. The region 1 (R1) FAC connects the inner edge of the boundary layer to the high-latitude edge of the auroral oval and the region 2 (R2) FAC connects the ring current to the low-latitude edge of the auroral oval. The R2 FAC is closed by an enhancement of the ring current (the *partial ring current*) on the midnight side of the Earth. The convection electric field between the ring current and the Earth is zero. See also Fig. 11.32

11.6.7 Coupling Between the Magnetosphere and the Ionosphere

Aurorae are caused by precipitation of energetic electrons into the ionosphere. The electrons collide with and excite atoms and molecules, notably O, N, and N_2, and visible light is emitted when these species decay back to the ground state.

Time-varying electric currents (the *solar disturbed,* or S_D, current system) associated with the aurora occur at altitudes between 100 and 150 km and cause significant Joule heating in the ionosphere. These currents are always present, and so are their attendant magnetic fields. As the ionospheric currents vary, their time-varying magnetic fields induce emfs in electric circuits on the ground and elsewhere. During particularly strong magnetic storms, these induced emfs can be powerful enough to disrupt power grids.

Here, we describe the S_D current system. Figure 11.35 is a perspective view of Fig. 11.32, showing the charge separation at the magnetopause boundary layer, the

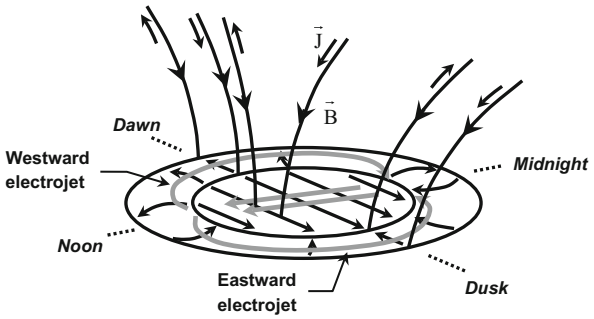

Fig. 11.36 Schematic diagram of ionospheric currents. The *arrows* beside the magnetic field lines are field-aligned (or Birkeland) currents; *black arrows* in the auroral oval and polar cap represent the directions of the electric field and the Pedersen current system; the *gray arrows* represent the Hall current system

resulting electrostatic fields, and some of the magnetic field lines coupling the magnetosphere to the northern ionosphere. These field lines also connect to the southern ionosphere (not shown in the diagram).

The boundary layer acts as a magnetohydrodynamic (MHD) generator: magnetospheric convection carries plasma antisunward through the Earth's magnetic field, creating a non-electrostatic field, $\vec{E}_{\mathrm{N}}$ that in turn produces a charge separation and a consequent electrostatic field, $\vec{E}_{\mathrm{E}}$ (cf. Sect. 11.6.5 and Fig. 11.32). The electromotive force (emf), ε, of this source may be calculated from

$$\varepsilon = \int \vec{E}_N \bullet \mathrm{d}\vec{\ell} = \int \left(\vec{v} \times \vec{B}\right) \bullet \mathrm{d}\vec{\ell} \tag{11.114}$$

and is typically 10–100 kV. The polarity of the source is as indicated in Figs. 11.32 and 11.35. The region just inside the boundary layer also acts as an MHD generator, with the opposite direction of magnetospheric convection and polarity of the emf.

Magnetospheric plasma is essentially collisionless, so the conductivity is very large parallel to $\vec{B}$ and very small perpendicular to $\vec{B}$. The magnetic field lines thus act as electrical conduits connecting the magnetospheric sources of emf to the ionospheric load. *Field-aligned currents* (called *Birkeland currents* in the Earth's magnetosphere, after their discoverer) then flow into and out of the ionosphere in the directions dictated by the polarity of the sources, as shown in Fig. 11.35. The current direction inside the magnetopause and magnetosphere in Fig. 11.35 is opposite to the electrostatic field, as required in a source of emf.

Figure 11.36 shows the magnetic and electrostatic fields and consequent current systems in the polar cap and auroral oval. Inspection of Figs. 11.35 and 11.36 shows that the dusk-to-dawn electric field in the boundary layer maps into the ionosphere as a dawn-to-dusk electric field in the polar cap, and the dawn-to-dusk electric field in the magnetosphere maps into the ionosphere as a dusk-to-dawn electric field in the auroral oval.

The electric and magnetic fields in the ionosphere create the Pedersen current system parallel to the electric field and the Hall current system antiparallel to the $\vec{E} \times \vec{B}$ direction (Sect. 11.5.7). The Pedersen current system has divergence (currents begin, end, or flow in opposite directions at boundaries) and is closed by the Birkeland currents to and from the magnetosphere, whereas the Hall current system is without divergence.

The Hall currents are more limited in spatial extent and therefore more intense in the auroral oval than in the polar cap and are referred to as electrojets (Fig. 11.36). During a moderately sized aurora, the electrojets can carry currents of several million amperes.

The idealized current orientation shown in Fig. 11.36 must be modified because electron precipitation results in a greater density of free charge and therefore conductivity in the auroral oval than in the polar cap. Because the Hall current is dominated by electrons drifting opposite to the current direction and the mobility of electrons is higher in the auroral oval (i.e., there is an impedance mismatch between the auroral oval and the polar cap), negative charge occurs where the Hall current enters the polar cap and a corresponding positive charge where the Hall current leaves the polar cap. The electrostatic field of these charges adds vectorially to the one shown in Fig. 11.36 to create a resultant electrostatic field directed from a point between midnight and dawn toward a point between noon and dusk. The (final) Pedersen current is parallel to the total electric field and the Hall current is perpendicular to it, so the Pedersen and Hall current systems are rotated clockwise (in the dawn to midnight direction) from the orientation shown in Fig. 11.36.

Fig. 11.37 shows the S_D current system at 2400 GMT averaged over a 12-month period in 1932–1933. Noon is downward. Note that the S_D current system is fixed relative to the Sun, and the Earth rotates counterclockwise under it. The westward electrojet is much stronger than the eastward and gives a maximum current density in the hours after midnight, above latitudes between 60° N and 70° N.

11.6.8 Magnetospheric Substorms

Magnetic substorms appear to be different in character and cause from magnetic storms (Sect. 11.6.4): (1) they are detected primarily at high geomagnetic latitudes, rather than worldwide as for magnetic storms; (2) the initial increase in $B_{\parallel}$ is lacking; (3) they tend to be stronger (i.e., deeper) but of much shorter duration than magnetic storms, typically 1–3 h; and (4) they often occur within a couple of hours after the vertical component of the IMF changes from northward to southward and stays that way. Point (2) shows that, unlike magnetic storms, enhancements of the solar wind are not involved, and (1) shows that the change in the ring current is much smaller than in magnetic storms.

Magnetic substorms can also occur during magnetic storms, but appear to differ from those described above, e.g., by injecting considerably more charged particles into the inner magnetosphere.

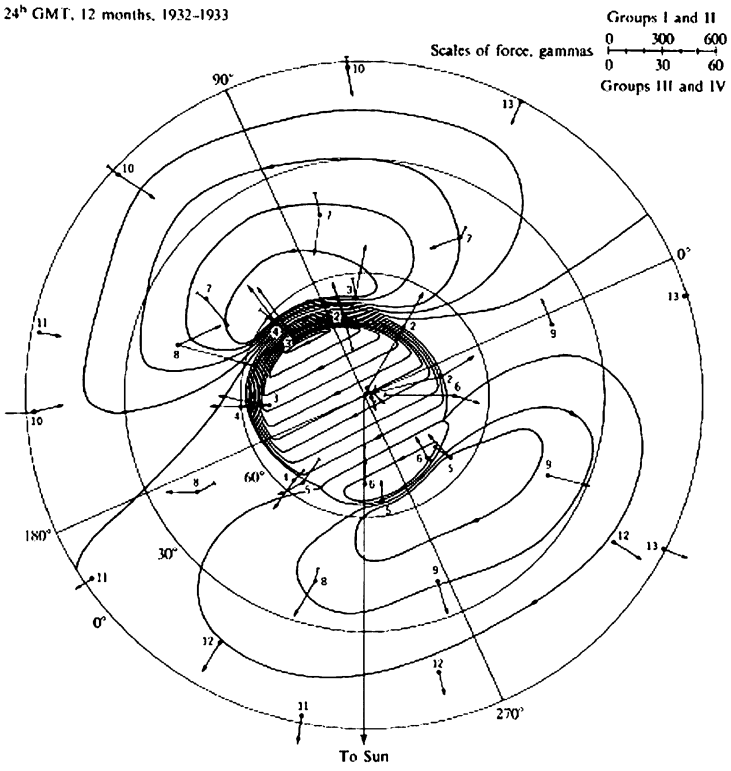

Fig. 11.37 The S_D ionospheric current systems. A current of 50,000 A flows between successive contours. Noon is towards the bottom. Current density is maximum shortly after local midnight. (From Silsbee and Vestine 1942, Fig. 8; and Parks 1991, Fig. 7.11, p. 281, with the latter's permission)

Figures 11.38 and 11.39 illustrate some aspects of the present picture of a magnetic substorm. When the IMF is southward, in the opposite direction to the planetary field, solar magnetic field lines can connect with those of the Earth near the dayside magnetic equator (Sergeev et al. 2012; Angelopoulos 2008; Milan et al. 2007). This process of *magnetic reconnection* converts closed, magnetospheric field lines into open field lines, which are then swept past the Earth and into the tail by the solar wind (Fig. 11.38). The loading of the tail with flux transported from the dayside magnetosphere increases the magnetic field strength in the tail by (typically) 10–30 %, and also increases the flaring of the tail (see Fig. 11.40b-d for an illustration of this phenomenon in Mercury's magnetotail). Because of the flaring, the solar wind ram pressure on the tail increases, compressing the plasma sheet; and when this becomes thin enough instabilities arise, causing:

(i) disruption of the cross-tail current near the Earth and the creation of field-aligned currents between there and the ionosphere (Fig. 11.39). The two

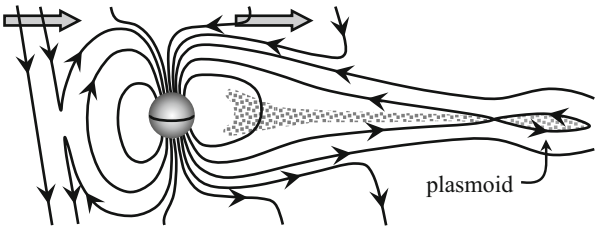

Fig. 11.38 Magnetic reconnection of southward IMF with the Earth's magnetic field at the dayside magnetospheric boundary. Magnetic reconnection also occurs in stretched magnetic field lines in the magnetotail, as described in the text

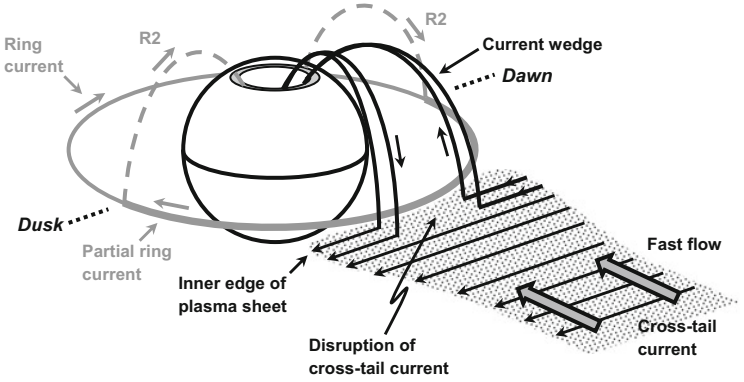

Fig. 11.39 Disruption of the cross-tail current at the inner edge of the plasma sheet and formation of the substorm current wedge to and from the ionosphere in the auroral oval (not to scale). Stippled region: plasma sheet; long, *black arrows*: cross-tail current; *thick arrows*: fast Earthward flow of plasma from the magnetotail. The region 2 (R2) currents joining the ring current to the auroral oval are also shown, in *grey*

field-aligned currents form a wedge-shaped structure when viewed from above the polar cap. This current wedge causes electrojet intensification and auroral breakup; i.e., a sudden expansion of the aurora with rapidly-moving curtains and other structures. The electrojet produces the magnetic signature of the substorm.

(ii) fast transport of plasma earthward along the neutral sheet from further out in the tail; and

(iii) magnetic reconnection of open magnetotail field lines across the neutral sheet (average distance ~18 R_E, where R_E is the radius of the Earth). The reconnection closes the field lines on the earthward side and creates detached regions of plasma and magnetic field called *plasmoids* on the tailward side (Fig. 11.38). The plasmoids convect tailward (away from the Earth) while the reconnected field line and associated plasma convect Earthward.

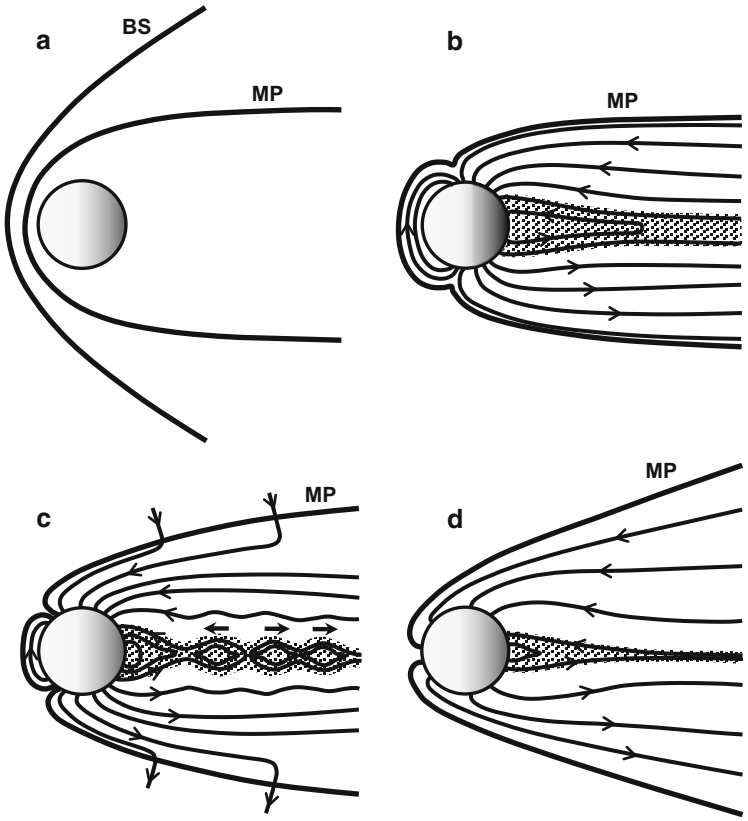

Fig. 11.40 The magnetosphere of Mercury. BS = bow shock; MP = magnetopause; stippled regions = magnetotail plasma sheet. North is upward and the Sun is to the left. (**a**) The mean configurations of the bow shock and magnetopause relative to the size of Mercury, approximately to scale. (**b**) Mercury's magnetopause, magnetosphere and plasma sheet under conditions of northward IMF. (**c**) Magnetopause and magnetosphere under conditions of southward IMF. (**d**) Magnetopause and magnetosphere under conditions of southward IMF and extreme loading by the solar wind. (**a**–**c**) Adapted from Slavin et al. 2012, Figs. 1 and 10, modified by permission of the American Geophysical Union; (**d**) Adapted from Slavin et al. 2010, Fig. 4, by permission of the authors and publisher

The order of points (i)–(iii), above, is still uncertain because they occur within ~1 min of each other (Angelopoulos 2008). It is possible that the current disruption occurs first, resulting in plasma flow and magnetic reconnection (an inside-out scenario), or reconnection may occur first, resulting in plasma flow and current disruption (an outside-in scenario).

This cycle in which open field lines are created by magnetic reconnection at the dayside magnetopause, swept into the magnetotail where they are reconnected, and swept back toward the Earth and into the dayside magnetosphere again is referred to as the *Dungey cycle*. The typical cycle time in the terrestrial magnetosphere is ~1 h.

It is also instructive to consider the Dungey cycle in terms of energy. Solar wind kinetic energy is converted to energy stored as magnetic flux in the magnetotail via dayside reconnection and transport of magnetic field lines into the magnetotail. The stored energy in the magnetotail is then converted into heat via magnetic reconnection, plasma transport and dissipation (heating) in the magnetotail, and dissipation in the electrojet. The magnetosphere therefore acts in part as a heat engine, converting solar wind kinetic energy into heat.

11.7 Magnetospheres of Mercury, Venus, and Mars

11.7.1 Mercury

Mercury's magnetosphere was probed by the *Mariner 10* spacecraft in its first and third flybys in 1974 and 1975 (the second flyby was at a distance of 48,000 km, too distant to obtain magnetospheric measurements), and by the *MESSENGER* spacecraft in three flybys in 2008 and 2009. *MESSENGER* entered orbit around Mercury on March 18, 2011 and began making more continuous observations of the magnetosphere (Sect. 9.1.3).

Mercury was found by *Mariner 10* to have a global magnetic field with characteristics best explained by an active core dynamo, and this picture has been confirmed by *MESSENGER*. Mercury is thus, at present, the only terrestrial planet besides the Earth found to have an internally-generated magnetic field. Characteristics of this field as measured by *MESSENGER* (Anderson et al. 2011) are:

- Magnetic field strength at Mercury's surface: ~1 % of that at the Earth's surface.
- Polarity: Same as the Earth. Magnetic field lines are directed northward outside the planetary surface and southward along the rotation axis. Thus, the north-seeking pole of a compass on Mercury's surface would point north.
- Configuration: Primarily dipolar. The dipole term $g_{10} = -195 \pm 10$ nT, giving a dipole moment $\mu = |g_{10}| R_M^3 = 2.83 \times 10^{12}$ T m^3, where R_M is Mercury's radius (2,440 km); dividing this value of μ by the quantity $\mu_0/4\pi$ yields 2.83×10^{19} amp m^2, or ~4×10^{-4} of that of the Earth.
- Axial tilt: $<3^\circ$ from the planetary rotation axis, or possibly not tilted at all. The Earth's magnetic dipole, by comparison, is tilted ~11° from the rotation axis.
- Dipole offset: Centered on the spin axis but displaced 484 ± 11 km north of the center of the planet. The corresponding quadrupole term is $g_{20} = -74 \pm 4$ nT, giving a ratio $g_{20}/g_{10} = 0.38$. (The larger this ratio, the more the center of the dipole is offset north or south of the planet center along the rotation axis.)

The only other planet with an axially-aligned dipole is Saturn, for which $g_{20}/g_{10} = 0.072$; i.e., the dipole offset is a factor of 5 greater for Mercury than for Saturn, relative to the planetary diameter. Thus, with its axially-aligned dipole and large dipole offset, Mercury's magnetic field is distinct from that of any other planet.

11.7.1.1 Magnetospheric Dynamics

Mean distances from planet center are 1.3 R_M to the magnetopause nose (the closest point of the magnetopause to Mercury's surface) and 1.7 R_M to the bow shock (Slavin et al. 2010). Figure 11.40a shows the mean configurations of the magnetopause and bow shock relative to the planet, approximately to scale. Because of Mercury's weak magnetic field, however, these boundaries vary significantly with the solar wind strength and IMF direction, as illustrated in Figs. 11.40b, c and d; e.g., the mean magnetopause position during northward IMF is ~1.5 R_M.

Figure 11.40b shows a typical magnetospheric configuration when the IMF has a northward component (toward the top of the page). In this case, the entire surface of Mercury is protected from the solar wind by the magnetosphere, the tail shows minimal flaring, and the plasma sheet has maximum thickness.

Figure 11.40c shows a typical magnetospheric configuration when the IMF has a southward component (toward the bottom of the page) (Slavin et al. 2010). As in the Earth's magnetosphere during southward IMF, magnetic reconnection takes place near the dayside magnetic equator and the solar wind sweeps the resulting open field lines past the planet and into the tail, loading the tail with magnetic flux and compressing the plasma sheet (Sect. 11.6.8 and Fig. 11.38). When this sheet becomes sufficiently thin it becomes unstable, giving rise to substorm-like behavior with magnetic reconnection in the tail, ejection of plasmoids, and plasma flow toward the planet.

Typical reconnection rates at Mercury's magnetopause are ~10 times those at the Earth (Slavin et al. 2012), probably because of the stronger IMF, and flux loading increases the magnetic field strength in the magnetotail lobes by as much as a factor of ~2, compared to 10–30 % for the Earth. The Dungey cycle time is ~1–2 min, compared to ~1 h for the Earth, ~1 week for Saturn, and ~1 month for Jupiter.

With southward IMF, the dayside reconnection significantly reduces the altitude of the dayside magnetopause and displaces the cusps at the magnetic poles toward the equator (Fig. 11.40c). Under extreme conditions, 100 % of the planet's magnetic flux can be transferred to the tail (Slavin et al. 2010). In this case, the two cusps merge into a single, broad cusp at the equator (Fig. 11.40d). This extreme configuration is expected to be highly unstable, and substorm-like behavior will quickly transfer magnetic flux back to the dayside on the Dungey cycle timescale.

The strong resemblance of Mercury's magnetospheric processes to those of the Earth suggests that there could also be a similar set of field-aligned currents (FACs); and indeed a region 1-type FAC of ~1.4×10^6 A has been observed at the magnetopause, along the boundary between the open field lines in the polar cusp and the closed field lines in the magnetosphere. However, there is a problem: On Mercury, in order to close the circuit (Lyatsky et al. 2010), a current of this magnitude requires a load whose conductance is ~35 S (1 S = 1 siemens = 1 mho, the SI unit of conductance, and the inverse of resistance). On the Earth, the ionosphere provides the load, but Mercury's extremely tenuous ionosphere (predominantly Na^+ and Mg^+ with a number density of only ~10 cm^{-3}) can provide

a height-integrated Pedersen conductance of only ~5 × 10^{-6} S, far too small to sustain the current observed. Two other suggested possibilities also appear to be ruled out (Lyatsky et al. 2010 and references therein):

- Ion pick-up conductance due to ionization and subsequent $\vec{E} \times \vec{B}$ drift of atoms sputtered from Mercury's surface by the solar wind. However, the maximum pick-up conductance is expected to be ~0.2 S which, while much higher than the classical ionospheric conductance, is still two orders of magnitude too low.
- Surface conductivity. However, if Mercury's crust has a similar conductivity to that of the lunar crust, then the maximum surface conductance is likely to be ~0.1 S, which again is insufficient.

Lyatsky et al. (2010) show that Alfvén waves (transverse plasma oscillations in which the ions provide the inertia and the magnetic field provides the restoring force) may be capable of providing the required closure for the FACs.

11.7.1.2 Particle Trapping

The Earth's Van Allen radiation belts (Sect. 11.6.3.3) consist of high-energy (keV to MeV) protons and electrons gyrating around magnetic field lines and mirroring back and forth between the magnetic poles. Gradient and curvature drift in this population gives rise to the diamagnetic ring current parallel to the geomagnetic equator (Sect. 11.6.3.4). An equivalent trapping region around Mercury was not expected because, if we scale the Earth's magnetosphere to Mercury based on the respective magnetopause positions measured from planetary center, the trapping region would be located inside the planet ($r < 1R_M$).

Nevertheless, *MESSENGER* detected an increase in low-energy (1–10 keV) ions and electrons centered on Mercury's magnetic equator (Schriver et al. 2011) a short distance below the magnetopause (e.g., near 1.4 R_M for a magnetopause distance of 1.5 R_M), accompanied by a decrease in magnetic field strength by 5–50 nT. The magnetic field decrease indicates the presence of a diamagnetic current, which suggests that the keV particles form a ring current as described above. Only about 10 % of the particles make a complete drift orbit around the planet; the rest are lost either by precipitation at the planetary surface (the loss cone angle is ~30°) or by escaping through the magnetopause. For this reason, the particles are referred to as *quasi-trapped*. The distances to the surface and the magnetopause also limit their energies; e.g., protons of energy >20 keV gyrating around magnetic field lines at 1.4 R_M at the magnetic equator (B ~ 0.83 nT) will escape through a dayside magnetopause at 1.5 R_M. The mean lifetime of a quasi-trapped particle in Mercury's magnetosphere is a few minutes, compared to several days for even very-high-energy particles trapped in the Earth's magnetosphere.

To maintain a continuous population, the large loss rate must be balanced by a compensating rate of supply. The dominant source appears to be the planetward magnetospheric convection in the magnetotail plasma sheet.

11.7.1.3 Mercury's Weak Magnetic Field

Planetary dynamos are thought to operate on the principle of *magnetostrophic balance*, characterized by force balance between the Coriolis force, pressure gradient force, and Lorentz force (equation 11.53). The ratio of the Lorentz force to the Coriolis force (a quantity referred to as the *Elsasser number*, Λ) should therefore be of order 1. Dynamo models for Mercury that include magnetostrophic balance predict magnetic fields similar in strength to the Earth's field. In reality, however, Mercury's observed global magnetic field has a surface field strength $\sim 10^{-2}$ of that of the Earth and a dipole moment $\sim 10^{-4}$ of that of the Earth, and extrapolation of the observed external magnetic field to the dynamo region gives an Elsasser number $\Lambda \sim 10^{-4}$. Mercury's weak magnetic field, therefore, rather than being a simple consequence of a smaller, more slowly-rotating planet, has in fact proven quite difficult to model.

Two non-dynamo models that have been proposed (Wicht et al. 2007 and references therein) are,

1. Remanent crustal magnetism from a now-defunct early dynamo. Runcorn (1975) has shown that "for a shell of any thickness magnetized by a dipole at its centre, the latter field being subsequently removed . . ., the shell gives rise to zero dipole moment, because the polar regions . . . are exactly compensated by the greater volume of more weakly oppositely magnetized material in the equatorial regions," and "all harmonics of the field external to the shell completely vanish." E.g., Runcorn (1975) argues that the almost-zero dipole moment of the Moon *requires* a core dynamo at the time the crust formed.

   Runcorn's theorem applies only if the magnetization is linearly proportional to the magnetic field vector, $\vec{B}$. This is the case if the material is weakly susceptible to magnetization, such as olivine, pyroxene and hematite, but if it is strongly susceptible, such as magnetite or iron, then the magnetization depends nonlinearly on the magnetizing field, and the remanent field outside the shell is not zero (Crary and Bagenal 1998). Lunar and Martian materials are weakly magnetizable so Runcorn's theorem applies, but the situation is less clear for a highly-differentiated planet like Mercury because it depends on how much iron remains in the mantle and crust, and in what form.

   For remanent magnetism to be the source of Mercury's global field, therefore, either there would need to be substantial amounts of strongly-magnetizable material in layers outside the core that are below the Curie temperature, or conditions would need to be found to prevent large-scale uniformity in the magnetic response of the crust to the dynamo field, e.g., by eliminating either the polar or the equatorial contribution. It is difficult to see how the latter situation would arise, and the state of iron in Mercury's mantle and lower crust is difficult to evaluate at the present time.
2. Thermoelectric generator. In this model, topographic undulations at the core–mantle boundary give rise to temperature differences that in turn create a thermoelectric emf. Electric currents produced in the core and mantle by this

emf create a weak toroidal (i.e., zonal) magnetic field. If convection in the core is too slow to produce a classical self-sustaining dynamo, its passage through this toroidal field may nevertheless generate electric currents that in turn produce the observed weak, global field. The thermoelectric effects combined with slow convection thus create an electric generator rather than a self-sustaining dynamo.

It is also possible that a magnetostrophic dynamo does exist in the core, but conditions within the core prevent the full magnetic field from being expressed externally (Wicht et al. 2007 and references therein). Thermal conduction through Mercury's stable lithosphere is expected to be small enough that the heat flow through the core-mantle boundary is subadiabatic. Convection in the outer core would then be from chemical buoyancy due to a chemical gradient (Sect. 9.1.4) rather than thermal buoyancy due to an adiabatic temperature gradient. In this case, most of the outer core could be convectively stable, with convection occurring in only a thin shell outside the inner core. If the dynamo in this shell varies with time, then the changes in the magnetic field will take time to diffuse through the conducting outer core. (See Sect. 8.5.3 for an example of diffusion of magnetic field through a conducting medium.) If the field in the dynamo region is dominated by multipole components, then the rapidly-varying higher-order components will be strongly attenuated in the external field and the external field will be dominated by the weaker, more slowly-varying dipole and quadrupole components, as observed.

Another possibility is that negative feedback from the diamagnetic boundary current, or Chapman-Ferraro current, at the dayside magnetopause (Sect. 11.6.2) limits the strength of the core dynamo (Heyner et al. 2011). Application of the right-hand rule to the Chapman-Ferraro current in Fig. 11.24 shows that the magnetic field of this current is from south to north inside the planet's core, opposite to the dipole field of the core dynamo. Numerical simulations show that the negative feedback provided by this process can limit the global field of the dynamo to small values, but only if the dynamo is weak to begin with. Mercury is expected to have had a vigorously-convecting core when it first formed, and therefore a strong primordial dynamo. It is likely that this convection and dynamo died out as Mercury cooled. Later, as cooling continued, the inner core began to form and convection restarted. If the dynamo increased gradually, then negative feedback could possibly prevent the dynamo and global magnetic field from growing past their present low values.

11.7.2 Venus

11.7.2.1 Internal Magnetic Field

No internally generated magnetic field has yet been detected around Venus. The upper limit on the magnetic dipole moment set by the *Magellan* orbiter is 1.5×10^{-5} that of the Earth.

Slow rotation (sidereal rotation period = 243 days, retrograde) has sometimes been cited as the reason why Venus has no observed intrinsic magnetic field, but in fact all of the terrestrial planets have more than enough rotation to create an electric dynamo if the structural and thermal conditions are met (Stevenson 2003 and references therein). However, because Venus is not rotationally distorted, its interior structure cannot be investigated by the evolution of spacecraft orbits. Consequently, the interior structure of Venus is poorly constrained by observations, and it is not known how much, if any, of the core is solid.

If the lack of an observed field arises from a lack of convection in the core, then the two most likely reasons are (1) the core is entirely molten or (2) there is a solid, inner core, but convection is suppressed. A completely molten core could occur if the impurity concentration is greater than in the Earth's core or may simply be a result of the lower central pressure compared to the Earth, because of the smaller planetary mass and radius (Stevenson et al. 1983).

Even if there is a solid, inner core, convection may be suppressed in the outer core (Nimmo 2002). The absence of plate tectonics, which is the dominant heat flow mechanism in the Earth's lithosphere, reduces the heat flow to space from Venus' interior (Sects. 9.2.7 and 9.2.8). This results in a hotter mantle and therefore a smaller temperature gradient in the outer core. If this temperature gradient is subadiabatic, then there will be no thermal convection.

If the catastrophic resurfacing model (Milone and Wilson 2014, Sect. 9.2.8) is correct, then low heat flow may alternate with periods of high heat flow. In this case, the absence of a global magnetic field may be a temporary, or possibly cyclic, property of Venus.

11.7.2.2 Induced Magnetosphere

Despite the absence of an internally driven magnetosphere, the interaction of the solar wind and IMF with Venus' ionosphere creates a magnetic obstacle that deflects the solar wind around the planet. Figure 11.41 illustrates some of the processes involved. The IMF can be regarded as frozen into the solar wind plasma and carried toward Venus at the solar wind velocity, $\vec{v}_{SW}$.

The motion of the IMF toward Venus at velocity $\vec{v}_{SW}$ is equivalent to the motion of the Venus ionospheric conductor through the IMF at velocity $-\vec{v}_{SW}$: a motional electric field and current are induced in the ionosphere as shown in Fig. 11.41. The induced magnetic field, $\vec{B}_{IND}$, adds to $\vec{B}_{IMF}$ on the sunward side of this current, increasing the magnetic field strength above the ionosphere, and opposes it on the side toward Venus. Thus, the magnetic field pressure

$$P_{IMF} = \frac{B_{IMF}^2}{8\pi}$$

increases in the region above the ionosphere, while the ionosphere is compressed by the incoming solar wind plasma and IMF. These processes are evident in passages

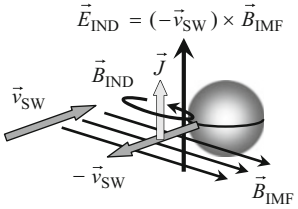

Fig. 11.41 The flow of IMF towards the ionospheric conductor induces a northwards current in the ionosphere for the IMF direction shown

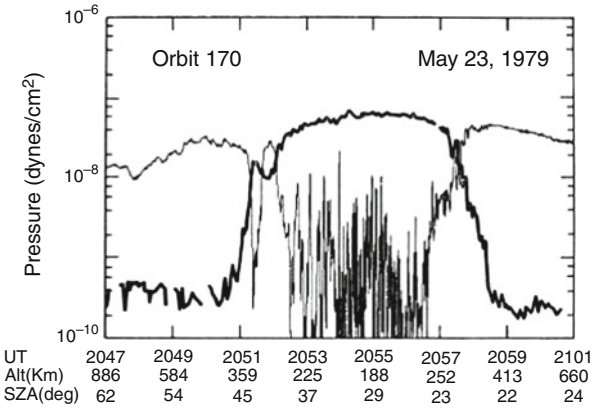

Fig. 11.42 Magnetic field pressure (*light lines*) and ionospheric plasma pressure *(heavy lines*) vs. altitude from one passage of *Pioneer Venus* through the midday ionosphere (Elphic et al. 1980, Fig. 6, p. 7683; copyright 1980, American Geophysical Union. Reproduced by permission of American Geophysical Union.)

of *Pioneer Venus* through the midday ionosphere: with increasing altitude, the ionospheric electron density drops to near zero in the same region where the magnetic field strength increases from near zero to a value somewhat elevated above that far from Venus (see Fig. 12, p. 892, Russell and Vaisberg 1983). Balance is achieved when the inward force due to the magnetic pressure at the ionopause, the outer boundary of the ionosphere, equals the outward force due to the ionospheric plasma pressure. This is illustrated in Fig. 11.42, where magnetic field pressure and ionospheric plasma pressure measured by *Pioneer Venus* are plotted against altitude above the surface of Venus.

If the ionosphere were superconducting, the IMF would be completely excluded, and the magnetic field would be zero below the ionopause. Instead, the spikes in Fig. 11.42 suggest that magnetic field enters the Venus atmosphere in localized "flux ropes."

The altitude of the ionopause depends on the solar wind strength. When the solar wind strength is low, the ionopause is at high altitudes where individual ions follow their own trajectories. The result is a diamagnetic current similar in physical cause to the Earth's boundary current, except that instead of solar wind ions moving toward the right into an internally generated magnetic field in Fig. 11.24, ionospheric ions in Fig. 11.41 move toward the left into the IMF (in the solar wind frame). Because the IMF is horizontal and eastward in the figure, the diamagnetic current is northward.

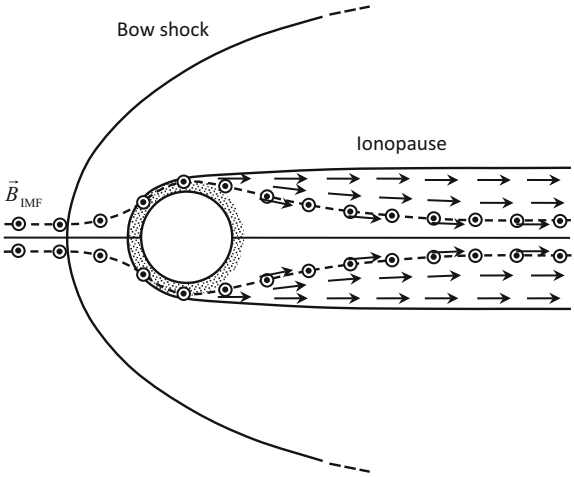

Fig. 11.43 IMF flow around Venus, viewed from the plane of the local IMF. The *circled dots* show magnetic field lines oriented toward the observer, and the *arrows* show the flow of low-energy ionospheric ions. Based on Russell and Vaisberg (1983), Fig. 18, p. 901

When the solar wind strength is high, the ionopause descends to lower altitudes and higher densities, where collisions occur. Whereas diamagnetic currents are dissipationless, collisions produce dissipation, and the current becomes an actual flow of charge in a resistive medium.

With the IMF effectively excluded from the ionosphere, the solar wind is deflected northward and southward past the planet, carrying the IMF with it (Figs. 11.42 and 11.43), forming a magnetocavity downwind from the planet where solar wind ions are excluded. The magnetic polarity in this cavity varies with the orientation of the IMF, unlike the magnetotails of planets with intrinsic magnetic fields. As with internally generated magnetospheres, a bow shock forms where the solar wind is slowed to subsonic speeds.

Solar rotation causes the outwardly-travelling IMF to form a spiral pattern around the Sun (referred to as the *Parker spiral*), in which the angle that the IMF makes with the radial direction from the Sun increases with distance from the Sun. This angle is 35° at Venus, 45° at the Earth, and 57° at Mars. This angle creates an asymmetry in Venus' magnetotail magnetic field, as shown in Fig. 11.43, with the field being stronger on one side of the tail than on the other.

In Fig. 11.43, the components of the magnetic field parallel to the magnetotail axis are oppositely-directed, and give rise to a cross-tail current and plasma sheet in a manner analogous to those in the Earth's magnetotail (Sect. 11.6.6). The induced electric field and current are directed out of the page (perpendicular to the magnetic field lines (Fig. 11.44)) for the magnetic field orientation shown in Fig. 11.43.

In an *induced magnetosphere*, such as that at Venus, the magnetic field direction is controlled by the direction of the IMF. Thus, processes that require the IMF to oppose the direction of the planetary field, including dayside reconnection, tailward flux transport, and magnetotail flux loading (Sect. 11.6.8), are absent in an induced magnetosphere. It was therefore somewhat surprising when *Venus Express* observed the magnetic and plasma-density signatures of plasmoids travelling

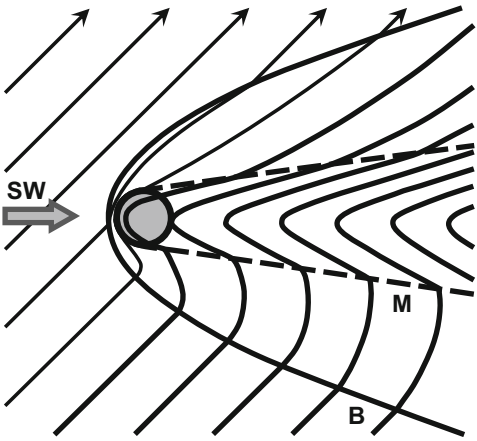

Fig. 11.44 IMF flow around Venus, viewed from above and perpendicular to the plane of the local IMF. *SW* solar wind direction; *B* bow shock; *M* magnetopause. Based on McComas et al. (1986), Fig. 1

toward the planet in Venus' magnetic tail (Zhang et al 2012), because in the case of the Earth and Mercury, plasmoids are created by magnetic reconnection in the magnetotail in response to flux loading. These plasmoids occur ~1–3 R_V down the tail from the planetary surface (where R_V is the radius of Venus) as the interplanetary field lines slip past Venus, and appear to be fairly common. The processes causing the reconnection are not yet clear.

11.7.2.3 Atmospheric Loss Rates

Measurements by *Pioneer Venus Orbiter* near solar maximum and more recently by *Venus Express* near solar minimum have shown that atmospheric loss from Venus is dominated by nonthermal escape of H^+ and O^+. The loss rates from *Venus Express* are 7.1×10^{24} s^{-1} for H^+ and 2.7×10^{24} s^{-1} for O^+ (Fedorov et al. 2011), with an estimated factor of 2 uncertainty in each value. The major ion acceleration processes are, (i) ion pick-up by the convecting magnetic field, (ii) magnetohydrodynamic plasma instabilities at the induced magnetosphere boundary, and (iii) polarization electric fields (i.e., electric fields caused by charge separations) oriented radially at low altitudes in the nightside ionosphere. The ions flow away from the planet primarily along the magnetotail plasma sheet and magnetotail boundary.

The hydrogen loss rate by Jeans escape of 2.5×10^{19} s^{-1} (Sect. 11.2.5.1) is negligible compared to the nonthermal rate above.

Neutral H and O also escape. Hot (i.e., energetic) H atoms are produced with sufficient energy to escape by (11.28)–(11.31), (11.34), (11.36) and other reactions. Hot O with sufficient energy to escape is produced by sputtering, as follows (Lammer et al. 2006). Planetary oxygen atoms on the dayside are ionized, picked up by the IMF and accelerated toward the planet. They then undergo charge exchange reactions and become hot, neutral O travelling toward the planet.

Subsequent collisions with cold O can create outward-moving O with enough energy to escape. Loss rates of neutral H and O are 50 % and 25 %, respectively, of the H and O ion loss rates (Barabash et al. 2007). Pickup ions from the hot H and O coronae also contribute to the atmospheric loss, but these rates are much smaller than those within the tail.

The loss of H and O from Venus' atmosphere is equivalent to a loss of water, so the ratio of the number of H atoms that escape per second to the number of O atoms would be expected to be 2:1. The observed numbers, above, give a ratio of $(1.5 \times 7.1 \times 10^{24}\ \mathrm{s}^{-1})/(1.25 \times 2.7 \times 10^{24}\ \mathrm{s}^{-1}) = 3.2 : 1$. Given the estimated factor of 2 uncertainties, this result is consistent with a 2:1 ratio.

The solar wind-ionosphere interaction on Venus has contributed significantly to atmospheric loss over the life of the planet. The dominant processes are (1) charge-exchange reactions and subsequent ion pick up by the IMF and (2) sputtering. In the former, solar wind ions and electrons ionize atomic H and O in the exosphere of Venus (e.g., $O + e^- \rightarrow O^+ + 2e^-$), and the resulting H^+ and O^+ are picked up by the IMF and carried off in the solar wind flow around the planet. In the latter, fast solar wind ions collide with neutral atoms in the exosphere or near the exobase. In the solar wind impact region, a cascade of collisions results in some atmospheric neutral atoms moving outward; in the solar wind flow around the planet, motion is tangential and a single collision can eject the atmospheric neutral.

11.7.3 Mars

11.7.3.1 Martian Magnetosphere

Of the many spacecraft to have visited Mars, the most accurate magnetic field measurements have been made by *Mars Global Surveyor* (*MGS*). *MGS* used aerobraking to refine its initial, highly elliptical orbit to a final, circular orbit at 400 km altitude, and in this process dipped into the Martian atmosphere, to altitudes as low as 101 km, to slow its orbital speed. In so doing, it became the first spacecraft to carry magnetometers below the Martian ionosphere, where the magnetic fields associated with the Martian crust and interior are stronger and the magnetometers are shielded from the external magnetic fields of the solar wind-ionosphere interaction (Sect. 11.7.2.2). Because of a solar panel anomaly, NASA extended the aerobraking period to ~18 months to reduce the force on the solar panels, allowing magnetometer readings to be taken over ~20 % of the Martian surface to much greater accuracy and higher resolution than is possible from the final 400 km mapping altitude.

To the limit of observations, Mars has no global magnetic field. *MGS* established an upper limit of 2×10^{17} A/m^2 for a global dipole moment, corresponding to a magnetic field strength at the Martian equator of 0.5 nT, about 10^{-6} that of the

Earth (Acuña et al. 2001); but the observations are in fact equally well represented by a dipole moment of zero. The interaction of the Martian atmosphere and ionosphere with the solar wind and IMF thus creates an induced magnetosphere, similar to that at Venus (Sect. 11.7.2.2).

A surprising and significant discovery by *MGS* is the existence of intense, localized remanent magnetism in the Martian crust (Connerney et al. 1999). Although some anomalies have been found in the younger, northern lowlands, by far the majority and the strongest occur in the ancient southern highlands. These anomalies appear in the *MGS* data as linear, approximately parallel, east–west-trending features up to 1,000–2,000 km in length and ~200 km in width, of alternating magnetic polarity. The 200 km width is imposed by the resolution of the *MGS* data, so in fact there could be finer lineations. Magnetic field strengths are up to ~1,500 nT at periapsis ($\geq$100 km altitude) and ~200 nT at the final mapping altitude of 400 km. These fields dwarf their terrestrial counterparts: the strongest crustal magnetic anomalies on the Earth produce variations of $\pm$10 nT in the dipole field at 400 km altitude. The dipole moment of (any) one 2,000 km long anomaly 200 km wide is an order of magnitude greater than that of the Kursk magnetic anomaly in Russia, one of the largest on the Earth.

The intense magnetization is consistent with the fact that the iron content of the Martian crust is much higher than on the Earth (17 % in the soil at the Pathfinder landing site and 15–30 % in Martian meteorites, compared to 1 % on the Earth), but it also requires a relatively intense inducing field, similar to or greater than that of the present-day Earth. The most likely model for this field is a global magnetic dipole created by an electric dynamo in a molten core. The timescale of this dynamo can be estimated from the fact that, within the southern highlands, magnetization tends to be absent in the material covering the large impact basins such as Argyre and Hellas. These are believed to have formed within the first 300 My of the accretion of Mars, suggesting that the dynamo died out during the earliest epoch on Mars. The scarcity and weakness of anomalies in the northern lowlands also suggests that the dynamo died out before the formation of the main north-south dichotomy of Mars; but it then becomes difficult to account for the anomalies that do exist there.

The most straightforward explanation for the linearity and alternating polarity of the anomalies is that they formed during an early period of plate tectonics, in which crustal spreading was accompanied by reversals of the putative Martian magnetic dipole as the spreading crust cooled below the Curie point. Although alternative explanations have not been ruled out, this model has an advantage of self-consistency in that plate tectonics increases the heat flux through the crust and thus the probability of core convection and an electric dynamo (Sect. 11.7.2.1). One requirement of the crustal spreading model is a symmetry axis analogous to mid-ocean ridges where new crust is being created on the Earth. None have yet been discovered, but large areas of the highlands have been reworked by impacts, thermal events, and fracturing, and such features may not have survived.

Mars is thus unique in the solar system in having both an induced magnetosphere and intrinsic magnetic fields associated with the crust. These crustal fields are strong enough to create small, magnetosphere-like cavities extending beyond

400 km altitude (the orbit of *Mars Global Surveyor*), and have magnetopause-like boundaries that exclude the solar wind and IMF from the cavity. These cavities rotate with the planet every 24 h, dynamically altering the induced magnetospheric structure of Mars.

The magnetic anomalies give rise to aurorae bright enough to be visible to the naked eye for an observer on the Martian surface (Lundin et al. 2007). The anomalies create a multipole magnetic field with closed field lines over the anomalies and open, cusp-like field lines between them. The aurorae occur ~50–80 km above the surface on "semi-open" flux tubes along the boundaries between the closed and open field lines, as do aurorae on the Earth. Field-aligned currents have been observed in these flux tubes, consisting of downward-accelerated electrons and upward-accelerated ionospheric ions (O^+, O_2^+ and CO_2^+). Precipitation of the electrons into the Martian atmosphere produces the aurorae.

Field-aligned currents require an acceleration mechanism in the magnetosphere to act as a source of emf. In the terrestrial magnetosphere, the acceleration is provided by magnetic reconnection across the plasma sheet in the magnetotail (Sect. 11.6.8), and Halekas et al. (2009) report 26 such events strong enough to have clear signatures in *MGS* magnetometer data. Given the complex interplay of solar wind, crustal, and draped magnetospheric field lines, it would not be surprising if magnetic reconnection occurs commonly at Mars and provides a source for the aurorae.

11.7.3.2 Atmospheric Loss Mechanisms

Atmospheric loss from Mars is dominated by loss of hydrogen and oxygen. Hydrogen loss in turn is dominated by Jeans escape, at a rate of ~2.2×10^{26} s^{-1} (Sect. 11.2.5.1). For comparison, the next important hydrogen loss mechanism is ion pickup, with a rate of 1.2×10^{25} s^{-1} for each of H^+ and H_2^+ (Lammer et al. 2003).

The rate of loss of H is set by the rate of supply of H_2 to the exosphere from below, which in turn is set by chemical reactions involving the dissociation of water. The loss mechanisms for hydrogen and oxygen are in fact mutually self-limiting: two H escape for each O (Lammer et al. 2003, and references therein). In effect, water molecules are being lost to space.

The stoichiometric 2:1 ratio in the loss of H and O requires an oxygen loss rate of ~1.1×10^{26} s^{-1}. (*Stoichiometric ratio* refers to the component elements being present in the exact proportion indicated by the chemical formula for the compound, in this case, H_2O.) Lammer et al. (2003) calculate an O^+ ion pickup rate of 3×10^{24} s^{-1}. Combined with dissociative recombination [via (11.21)] and sputtering rates from the literature of 5.0×10^{24} s^{-1} and 4.3×10^{23} s^{-1}, respectively, they obtain a total oxygen loss rate of 8.4×10^{24} s^{-1}. This is more than a factor of 20 lower than required by the stoichiometric ratio. Another sink is therefore required for oxygen, and the most likely candidate appears to be oxidation of the regolith. Meteoric gardening (excavation of fresh regolith and burial of older, oxidized regolith) is suspected to be sufficient to maintain an active sink.

With a loss rate of 1.1×10^{26} molecules s^{-1} over the life of Mars (~4.6×10^9 y), a surface layer of water ~2.5 m deep would have been lost. Greater solar UV flux in the early solar system might increase this to ~20 m. In fact, various Martian surface features (cf. Sect. 9.3.3 of Milone and Wilson 2014) may indicate a layer of water as much as 500 m deep when Mars was young, so other loss mechanisms may also have been important in the past.

The present Martian atmosphere contains only ~1/10,000 as much water as there is in the Earth's atmosphere. This amount is enough to cover the surface of Mars with a uniform layer of water only 10 μm thick. This has not always been so: The amount of water in the north polar remnant ice cap is ~10^5 times greater.

Challenges

[11.1] In (11.26), derive $\lambda_J = r_x/H_x$ and $\lambda_J = (v_{esc}/v_{th})^2$ from the expression $\lambda_J = GMm/(kT_x r_x)$.

[11.2] Derive (11.93) from (11.92). [Hint: Electric current equals the amount of charge passing a given point per second; how is the current associated with a gyrating particle related to the charge of the particle and the period of the gyromotion?]

[11.3] Derive (11.98) from (11.76) and other previous results.

[11.4] Justify, using $\vec{F}_B = q\vec{v} \times \vec{B}$, the statement preceding (11.99) that the kinetic energy of the particle is constant. [A descriptive answer is acceptable, but the description should be physically precise.]

[11.5] Spacecraft orbiting through the trapping region of a planetary magnetosphere, such as the Earth's Van Allen radiation belts, do not necessarily orbit in the plane of the magnetic equator; thus, they sample the magnetosphere at a range of magnetic latitudes. For uniformity of data, measured pitch angles are usually referred to the magnetic equator. If the spacecraft measures a pitch angle, α, for a particle at a location away from the magnetic equator where the magnetic field strength is B, and if *on the same field line* the magnetic field strength at the magnetic equator is B_0, show that the pitch angle, α_0, of the particle as it crosses the magnetic equator is given by

$$\sin^2\alpha_0 = \frac{B_0}{B}\sin^2\alpha$$

[Hint: μ_B and Φ_B are constants of the motion. Express the pitch angles in terms of $v_\perp$ at B and $v_\perp^0$ at B_0, and use (11.93) and (11.97).]

[11.6] The loss cone is approximately 3° for particles on the geomagnetic equator at 6 R_E above the Earth's surface, i.e., particles of this pitch angle mirror at ionospheric heights:

a. What is the mirror ratio, i.e., the ratio of the magnetic field strength at the ionosphere to that at the geomagnetic equator, along this field line? [Hint: Refer to problem 11.4. What is the pitch angle at the mirror point?]

Fig. 11.45

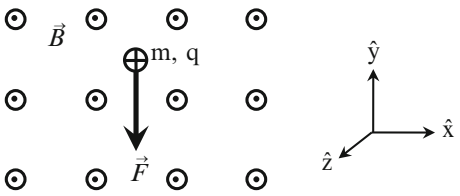

b. If particles are injected with an initially isotropic distribution of pitch angles at 6 R_E on the geomagnetic equator, what fraction of these particles are precipitated?

[11.7] Equations (11.77) and (11.79) in Sect. 11.5.6 give, respectively, the $\vec{F} \times \vec{B}$ drift velocity, $\vec{v}_D$, and its more commonly used form, the $\vec{E} \times \vec{B}$ drift velocity. The purpose of this problem is to derive (11.77) and (11.79).

Figure 11.45 shows a uniform magnetic field, $\vec{B}$, out of the page. In addition to any magnetic forces, all charges in this region also feel a downward force, $\vec{F}$, of external origin (e.g., gravitational or electrical) of uniform magnitude regardless of position. ($\vec{F}$ is unrelated to $\vec{B}$.)

a. Suppose you take hold of the charge shown above and run with a constant (vector) velocity, $\vec{v}$, holding tightly onto the charge so it cannot execute gyromotion. In what *direction* would you have to run so that the total force (or net force) on the particle is zero? Draw a vector diagram showing and labelling $\vec{B}, \vec{v}$, and all forces. Then write down the vector equation relating $\vec{F}, \vec{v}$, and $\vec{B}$. (In this and the other parts, below, keep careful track of minus signs.)
b. Evaluate the quantity $\left(\vec{v} \times \vec{B}\right) \times \vec{B}$ for this situation, using the unit vectors shown above. Express your answer in terms of a single unit vector, then rewrite your answer to express the quantity $\left(\vec{v} \times \vec{B}\right) \times \vec{B}$ in terms of $\vec{v}$.
c. Obtain (11.77) from your answers to parts a and b.
d. Now assume that the force, $\vec{F}$, is caused by an electric field vertically downward in the reference frame of the diagram (i.e., $\vec{F} = q\vec{E}$). In *your* reference frame, the force on a stationary particle is zero. It follows that, by running, you have placed yourself in a reference frame in which the electric field is zero: if you let go of the particle, it will remain at rest in your reference frame, so evidently there is no electric field.

   If a particle is now released at rest in the original reference frame of the diagram, what initial velocity will *you* see for this particle? What subsequent motion do you expect to see for this particle? (Remember, in your reference frame there is only a magnetic field.) By extension, what subsequent motion would an observer see who is at rest in the reference frame of the diagram? What is the $\vec{E} \times \vec{B}$ drift velocity of the guiding center in the reference frame of the diagram? (Also check that the drift velocity *is* in the direction of $\vec{E} \times \vec{B}$.)

References

Acuña, M.H., Connerney, J.E.P., Wasilewski, P., Lin, R.P., Mitchell, D., Anderson, K.A., Carlson, C.W., McFadden, J., Reme, H., Mazelle, C., Vignes, D., Bauer, S.J., Cloutier, P., Ness, N.F.: Magnetic field of Mars: summary of results from the aerobraking and mapping orbits. J. Geophys. Res. **106**(E10), 23403–23417 (2001)

Anderson, B.J., Johnson, C.L., Korth, H., Purucker, M.E., Winslow, R.M., Slavin, J.A., Solomon, S.C., McNutt Jr., R.L., Raines, J.M., Zurbuchen, T.H.: The global magnetic field of Mercury from MESSENGER orbital observations. Science **333**, 1859–1862 (2011)

André, M., Yau, A.: Theories and Observations of Ion Energization and outflow in the High latitude Magnetosphere. Space Sci. Rev. **80**, 27–48 (1997)

Angelopoulos, V.: The THEMIS Mission. Space Sci. Rev. **141**, 5–34 (2008)

Barabash, S., Fedorov, A., Sauvaud, J.J., Lundin, R., Russell, C.T., Futaana, Y., Zhang, T.L., Andersson, H., Brinkfeldt, K., Grigoriev, A., Holmström, M., Yamauchi, M., Asamura, K., Baumjohann, W., Lammer, H., Coates, A.J., Kataria, D.O., Linder, D.R., Curtis, C.C., Hsieh, K.C., Sandel, B.R., Grande, M., Gunell, H., Koskinen, H.E.J., Kallio, E., Riihelä, P., Säles, T., Schmidt, W., Kozyra, J., Krupp, N., Fränz, M., Woch, J., Luhmann, J., McKenna-Lawlor, S., Mazelle, C., Thocaven, J.-J., Orsini, S., Cerulli-Irelli, R., Mura, M., Milillo, M., Maggi, M., Roelof, E., Brandt, P., Szego, K., Winningham, J.D., Frahm, R.A., Scherrer, J., Sharber, J.R., Wurz, P., Bochsler, P.: The loss of ions from Venus through the plasma wake. Nature **450**, 650–653 (2007)

Cahill Jr., L.J.: Inflation of the inner magnetosphere. In: Carovillano, R.L., McClay, J.F., Radoski, H.R. (eds.) Physics of the Magnetosphere, pp. 263–270. Reidel, Dordrecht (1968)

Chen, R.H., Cravens, T.E., Nagy, A.F.: The Martian ionosphere in light of the Viking observations. J. Geophys. Res. **83**, 3871–3876 (1978)

Chaufray, J.Y., Bertaux, J.L., Leblanc, F., Quémerais, E.: Observation of the hydrogen corona with SPICAM on Mars Express. Icarus **195**, 598–613 (2008)

Connerney, J.E.P., Acuña, M.H., Wasilewski, P., Ness, N.F., Reme, H., Mazelle, C., Vignes, D., Lin, R.P., Mitchell, D., Cloutier, P.: Magnetic lineations in the ancient crust of Mars. Science **284**(5415), 794–798 (1999)

Crary, F.J., Bagenal, F.: Remanent ferromagnetism and the interior structure of Ganymede. J. Geophys. Res. **103**, E11, 25,757-25,773 (1998)

Elphic, R.C., Russell, C.T., Slavin, J.A., Brace, L.H.: Observations of the dayside ionopause and ionosphere of Venus. J. Geophys. Res. **85**, 7679–7696 (1980)

Fedorov, A., Barabash, S., Sauvaud, J.-A., Futaana, Y., Zhang, T.L., Lundin, R., Ferrier, C.: Measurements of the ion escape rates from Venus for solar minimum. J. Geophys. Res. **116**, A07220 (2011). doi:10.1029/2011JA016427 (9 pages)

Griffiths, D.J.: Introduction to Electrodynamics, 3rd edn. Prentice-Hall, Upper Saddle River, NJ (1999)

Halekas, J.S., Eastwood, J.P., Brain, D.A., Phan, T.D., Øieroset, M., Lin, R.P.: In situ observations of reconnection hall magnetic fields at Mars: evidence for ion diffusion region encounters. J. Geophys. Res. **114**, A11204 (2009). doi:10.1029/2009JA014544 (18 pages)

Heyner, D., Wicht, J., Gómez-Pérez, N., Schmitt, D., Auster, H.-U., Glassmeier, K.-H.: Evidence from numerical experiments for a feedback dynamo generating Mercury's magnetic field. Science **334**, 1690–1693 (2011)

Hunten, D.M.: Thermal and nonthermal escape mechanisms for terrestrial bodies. Planet. Space Sci. **30**(8), 773–783 (1982)

Hunten, D.M., Pepin, R.O., Walker, J.C.G.: Mass fractionation in hydrodynamic escape. Icarus **69**, 532–549 (1987)

Knudsen, D.J.: Private communication (2013)

Korte, M., Constable, C.: Improving geomagnetic field reconstructions for 0–3 ka. Phys. Earth Planet. In. **188**, 247–259 (2011)

Iribarne, J.V., Cho, H.-R.: Atmospheric Physics. Reidel, Dordrecht (1980)

Lammer, H., Lichtenegger, H.I.M., Biernat, H.K, Erkaev, N.V., Arshukova, I.L., Kolk, C., Gunell, H., Lukyanov, A., Holmstrom, M., Barabash, S., Zhang, T.L., Baumjohann, W.: Loss of hydrogen from the upper atmosphere of Venus. Planetary and Space Science **54**, 1445-1456 (2006)

Lammer, H., Lichtenegger, H.I.M., Kolb, C., Ribas, I., Guinan, E.F., Abart, R., Bauer, S.J.: Loss of water from Mars: implications for the oxidation of the soil. Icarus **165**, 9–25 (2003)

Lundin, R., Winningham, D., Barabash, S., Frahm, R., Brain, D., Nilsson, H., Holmström, M., Yamauchi, M., Sharber, J.R., Sauvaud, J.-A., Fedorov, A., Asamura, K., Hayakawa, H., Coates, A.J., Soobiah, Y., Curtis, C., Hsieh, K.C., Grande, M., Koskinen, H., Kallio, E., Kozyra, J., Woch, J., Fraenz, M., Luhmann, J., McKenna-Lawler, S., Orsini, S., Brandt, P., Wurz, P.: Auroral plasma acceleration above Martian magnetic anomalies. Space Sci. Rev. **126**, 333–354 (2007)

Lyatsky, W., Khazanov, G.V., Slavin, J.A.: Alfven Wave Reflection model of field-aligned currents at Mercury. Icarus **209**, 40–45 (2010)

McComas, D.J., Spence, H.E., Russell, C.T., Saunders, M.A.: The average magnetic field draping and consistent plasma properties of the Venus magnetotail. J. Geophys. Res. **91**(A7), 7939–7953 (1986)

Milan, S.E., Provan, G., Hubert, B.: Magnetic flux transport in the Dungey Cycle: a survey of dayside and nightside reconnection rates. J. Geophys. Res. **112**, A01209 (2007). doi:10.1029/2006JA011642 (13 pages)

Milone, E.F., Wilson, W.J.F.: Solar System Astrophysics: Planetary Atmospheres and the Outer Solar System, 2nd edn. Springer, New York (2014)

Nair, H., Allen, M., Anbar, A.D., Yung, Y.L.: A photochemical model of the Martian atmosphere. Icarus **111**, 124–150 (1994)

Nimmo, F.: Why does Venus lack a magnetic field? Geology **3**(11), 987–990 (2002)

Olson, P., Deguen, R.: Eccentricity of the geomagnetic dipole caused by lopsided inner core growth. Nature Geoscience **5**, 565-569 (2012)

Parks, G.K.: Physics of Space Plasmas, an Introduction. Addison-Wesley, Redwood City, CA (1991)

Parks, G.K.: Physics of Space Plasmas, an Introduction. 2nd ed. Harper-Collins, Perseus Books, Reading, MA (2003)

Runcorn, S.K.: An ancient lunar magnetic dipole field. Nature **253**, 701–703 (1975)

Russell, C.T., Vaisberg, O.: The interaction of the solar wind with Venus. In: Hunten, D.M., Colin, L., Donahue, T.M., Moroz, V.I. (eds.) Venus, pp. 873–879. University of Arizona Press, Tucson, AZ (1983)

Schriver, D., Trávníček, P.M., Anderson, B.J., Ashour-Abdalla, M., Baker, D.N., Benna, M., Boardsen, S.A., Gold, R.E., Hellinger, P., Ho, G.C., Korth, H., Krimigis, S.M., McNutt Jr., R.L., Raines, J.M., Richard, R.L., Slavin, J.A., Solomon, S.C., Starr, R.D., Zurbuchen, T.H.: Quasi-trapped ion and electron populations at Mercury. Geophys. Res. Lett. **38**, L23103 (2011). doi:10.1029/2011GL049629 (6 pages)

Sergeev, V.A., Angelopoulos, V., Nakamura, R.: Recent advances in understanding substorm dynamics. Geophys. Res. Lett. **39**, L05101 (2012). doi:10.1029/2012GL050859 (10 pages)

Silsbee, H., Vestine, E.: Geomagnetic bays, their frequency and current systems. Terr. Magn. Atmos. Electr. **47**, 195–208 (1942)

Slavin, J.A., Anderson, B.J., Baker, D.N., Benna, M., Boardsen, S.A., Gold, R.E., Ho, G.C., Imber, S.M., Korth, H., Krimigis, S.M., McNutt Jr., R.L., Raines, J.M., Sarantos, M., Schriver, D., Solomon, S.C., Trávníček, P., Zurbuchen, T.H.: MESSENGER and Mariner 10 Flyby observations of magnetotail structure and dynamics at Mercury. *J. Geophys. Res.* **117**, A01215 (2012). doi:10.1029/2011JA016900 (4 pages)

Slavin, J.A., Anderson, B.J., Baker, D.N., Benna, M., Boardsen, S.A., Gloeckler, G., Gold, R.E., Ho, G.C., Korth, H., Krimigis, S.M., McNutt Jr., R.L., Nittler, L.R., Raines, J.M., Sarantos, M., Schriver, D., Solomon, S.C., Starr, R.D., Trávníček, P.M., Zurbuchen, T.H.: MESSENGER observations of extreme loading and unloading of Mercury's magnetic tail. Science **329**, 665–668 (2010)

Stevenson, D.J.: Planetary magnetic fields. Earth Planet. Sci. Lett. **208**, 1–11 (2003)
Stevenson, D.J., Spohn, T., Schubert, G.: Magnetism and thermal evolution of the terrestrial planets. Icarus **54**, 466–489 (1983)
Vasyliūnas, V.M., Song, P.: Meaning of ionospheric Joule heating. J. Geophys. Res. **110**, A02301 (2005). doi:10.1029/2004JA010615 (8 pages)
Wicht, J., Mandea, M., Takahashi, F., Christensen, U.R., Matsushima, M., Langlais, B.: The origin of Mercury's internal magnetic field. Space Sci. Rev. **132**, 261–290 (2007)
Zhang, T.L., Lu, Q.M., Baumjohann, W., Russell, C.T., Fedorov, A., Barabash, S., Coates, A.J., Du, A.M., Cao, J.B., Nakamura, R., Teh, W.L., Wang, R.S., Dou, X.K., Wang, S., Glassmeier, K.H., Auster, H.U., Balikhin, M.: Magnetic reconnection in the near Venusian magnetotail. Science **336**, 567–570 (2012)

http://www.springer.com/978-1-4614-9089-0

Solar System Astrophysics
Planetary Atmospheres and the Outer Solar System
Milone, E.F.; Wilson, W.J.F.
2014, XVIII, 480 p. 188 illus., 27 illus. in color.,
Hardcover
ISBN: 978-1-4614-9089-0